The JCMT BISTRO Survey: Alignment between Outflows and Magnetic Fields in Dense Cores/Clumps

Hsi-Wei Yen[1] , Patrick M. Koch[1] , Charles L. H. Hull[2,3,43] , Derek Ward-Thompson[4] , Pierre Bastien[5], Tetsuo Hasegawa[6] , Woojin Kwon[7,8] , Shih-Ping Lai[1,9] , Keping Qiu[10,11] , Tao-Chung Ching[12,13] , Eun Jung Chung[14] , Simon Coudé[15] , James Di Francesco[16,17], Pham Ngoc Diep[18], Yasuo Doi[19] , Chakali Eswaraiah[13] , Sam Falle[20], Gary Fuller[21] , Ray S. Furuya[22,23] , Ilseung Han[8,24], Jennifer Hatchell[25] , Martin Houde[26] , Shu-ichiro Inutsuka[27] , Doug Johnstone[16,17] , Ji-hyun Kang[8] , Miju Kang[8] , Kee-Tae Kim[8,24] , Florian Kirchschlager[28] , Jungmi Kwon[29] , Chang Won Lee[8,24] , Chin-Fei Lee[1] , Hong-Li Liu[30,31,32] , Tie Liu[32,33] , A-Ran Lyo[8] , Nagayoshi Ohashi[1], Takashi Onaka[29,34] , Kate Pattle[35] , Sarah Sadavoy[36] , Hiro Saito[37], Hiroko Shinnaga[38] , Archana Soam[15] , Mehrnoosh Tahani[39], Motohide Tamura[29,40,41] , Ya-Wen Tang[1] , Xindi Tang[42] , and Chuan-Peng Zhang[12,13]

[1] Academia Sinica Institute of Astronomy and Astrophysics, 11F of Astro-Math Bldg, 1, Section 4, Roosevelt Road, Taipei 10617, Taiwan; hwyen@asiaa.sinica.edu.tw
[2] National Astronomical Observatory of Japan, NAOJ Chile, Alonso de Córdova 3788, Office 61B, 7630422, Vitacura, Santiago, Chile
[3] Joint ALMA Observatory, Alonso de Córdova 3107, Vitacura, Santiago, Chile
[4] Jeremiah Horrocks Institute, University of Central Lancashire, Preston PR1 2HE, UK
[5] Centre de recherche en astrophysique du Québec & département de physique, Université de Montréal, C.P. 6128 Succ. Centre-ville, Montréal, QC, H3C 3J7, Canada
[6] National Astronomical Observatory of Japan, National Institutes of Natural Sciences, Osawa, Mitaka, Tokyo 181-8588, Japan
[7] Department of Earth Science Education, Seoul National University, 1 Gwanak-ro, Gwanak-gu, Seoul 08826, Republic of Korea
[8] Korea Astronomy and Space Science Institute, 776 Daedeokdae-ro, Yuseong-gu, Daejeon 34055, Republic of Korea
[9] Institute of Astronomy and Department of Physics, National Tsing Hua University, Hsinchu 30013, Taiwan
[10] School of Astronomy and Space Science, Nanjing University, 163 Xianlin Avenue, Nanjing 210023, People's Republic of China
[11] Key Laboratory of Modern Astronomy and Astrophysics (Nanjing University), Ministry of Education, Nanjing 210023, People's Republic of China
[12] CAS Key Laboratory of FAST, National Astronomical Observatories, Chinese Academy of Sciences, People's Republic of China
[13] National Astronomical Observatories, Chinese Academy of Sciences, A20 Datun Road, Chaoyang District, Beijing 100012, People's Republic of China
[14] Department of Astronomy and Space Science, Chungnam National University, 99 Daehak-ro, Yuseong-gu, Daejeon 34134, Republic of Korea
[15] SOFIA Science Center, Universities Space Research Association, NASA Ames Research Center, Moffett Field, CA 94035, USA
[16] NRC Herzberg Astronomy and Astrophysics, 5071 West Saanich Road, Victoria, BC V9E 2E7, Canada
[17] Department of Physics and Astronomy, University of Victoria, Victoria, BC V8W 2Y2, Canada
[18] Vietnam National Space Center, Vietnam Academy of Science and Technology, 18 Hoang Quoc Viet, Hanoi, Vietnam
[19] Department of Earth Science and Astronomy, Graduate School of Arts and Sciences, The University of Tokyo, 3-8-1 Komaba, Meguro, Tokyo 153-8902, Japan
[20] Department of Applied Mathematics, University of Leeds, Woodhouse Lane, Leeds LS2 9JT, UK
[21] Jodrell Bank Centre for Astrophysics, School of Physics and Astronomy, University of Manchester, Oxford Road, Manchester M13 9PL, UK
[22] Tokushima University, Minami Jousanajima-machi 1-1, Tokushima 770-8502, Japan
[23] Institute of Liberal Arts and Sciences Tokushima University, Minami Jousanajima-machi 1-1, Tokushima 770-8502, Japan
[24] University of Science and Technology, Korea, 217 Gajeong-ro, Yuseong-gu, Daejeon 34113, Republic of Korea
[25] Physics and Astronomy, University of Exeter, Stocker Road, Exeter EX4 4QL, UK
[26] Department of Physics and Astronomy, The University of Western Ontario, 1151 Richmond Street, London N6A 3K7, Canada
[27] Department of Physics, Graduate School of Science, Nagoya University, Furo-cho, Chikusa-ku, Nagoya 464-8602, Japan
[28] Department of Physics and Astronomy, University College London, London WC1E 6BT, UK
[29] Department of Astronomy, Graduate School of Science, The University of Tokyo, 7-3-1 Hongo, Bunkyo-ku, Tokyo 113-0033, Japan
[30] Department of Astronomy, Yunnan University, Kunming, 650091, People's Republic of China
[31] Departamento de Astronomía, Universidad de Concepción, Av. Esteban Iturra s/n, Distrito Universitario, 160-C, Chile
[32] Shanghai Astronomical Observatory, Chinese Academy of Sciences, 80 Nandan Road, Shanghai 200030, People's Republic of China
[33] Key Laboratory for Research in Galaxies and Cosmology, Shanghai Astronomical Observatory, Chinese Academy of Sciences, 80 Nandan Road, Shanghai 200030, People's Republic of China
[34] Department of Physics, Faculty of Science and Engineering, Meisei University, 2-1-1 Hodokubo, Hino, Tokyo 1191-8506, Japan
[35] Centre for Astronomy, School of Physics, National University of Ireland Galway, University Road, Galway, Ireland
[36] Department for Physics, Engineering Physics and Astrophysics, Queen's University, Kingston, ON K7L 3N6, Canada
[37] Faculty of Pure and Applied Sciences, University of Tsukuba, 1-1-1 Tennodai, Tsukuba, Ibaraki 305-8577, Japan
[38] Department of Physics and Astronomy, Graduate School of Science and Engineering, Kagoshima University, 1-21-35 Korimoto, Kagoshima 890-0065, Japan
[39] Dominion Radio Astrophysical Observatory, Herzberg Astronomy and Astrophysics Research Centre, National Research Council Canada, P.O. Box 248, Penticton, BC V2A 6J9 Canada
[40] Astrobiology Center, 2-21-1 Osawa, Mitaka-shi, Tokyo 181-8588, Japan
[41] National Astronomical Observatory, 2-21-1 Osawa, Mitaka-shi, Tokyo 181-8588, Japan
[42] Xinjiang Astronomical Observatory, Chinese Academy of Sciences, 830011 Urumqi, People's Republic of China

Abstract

We compare the directions of molecular outflows of 62 low-mass Class 0 and I protostars in nearby (<450 pc) star-forming regions with the mean orientations of the magnetic fields on 0.05–0.5 pc scales in the dense cores/clumps where they are embedded. The magnetic field orientations were measured using the JCMT POL-2 data taken by the BISTRO-1 survey and from the archive. The outflow directions were observed with interferometers in the literature. The observed distribution of the angles between the outflows and the magnetic fields peaks between 15° and 35°. After considering projection effects, our results could suggest that the outflows tend to be misaligned with the magnetic fields by 50° ± 15° in three-dimensional space and are less likely (but not ruled out) randomly

---

[43] NAOJ Fellow.

oriented with respect to the magnetic fields. There is no correlation between the misalignment and the bolometric temperatures in our sample. In several sources, the small-scale (1000–3000 au) magnetic field is more misaligned with the outflow than the large-scale magnetic field, suggesting that the small-scale magnetic field has been twisted by the dynamics. In comparison with turbulent MHD simulations of core formation, our observational results are more consistent with models in which the energy densities in the magnetic field and the turbulence of the gas are comparable. Our results also suggest that the misalignment alone cannot sufficiently reduce the efficiency of magnetic braking to enable formation of the observed number of large Keplerian disks with sizes larger than 30–50 au.

Unified Astronomy Thesaurus concepts: Star formation (1569); Star forming regions (1565); Protostars (1302); Interstellar magnetic fields (845)

Supporting material: figure sets

1. Introduction

Star-forming regions are magnetized (Crutcher 2012; Planck Collaboration et al. 2016a). The magnetic field is theoretically expected to be dynamically important during the star formation processes (e.g., Galli & Shu 1993; Basu & Mouschovias 1994; Allen et al. 2003). On large scales, the relative importance of the magnetic field and the turbulence could affect structure formation in molecular clouds (McKee & Ostriker 2007; Soler et al. 2013) as well as the properties of dense cores formed in them (e.g., Burkert & Bodenheimer 2000; Gammie et al. 2003). Inside dense cores, the magnetic field could influence the transfer of mass and angular momentum from large to small scales and subsequently the formation and evolution of circumstellar disks around protostars (Li et al. 2014). Therefore, observational studies of magnetic field structures in comparison with other physical quantities in a large sample of molecular clouds and dense cores are essential to understand the role of the magnetic field in star formation (e.g., Matthews et al. 2009; Palmeirim et al. 2013; Poidevin et al. 2013; Koch et al. 2014; Zhang et al. 2014; Planck Collaboration et al. 2016b; Hull & Zhang 2019; Pattle & Fissel 2019; Chen et al. 2020).

Alignment between the magnetic field and rotational axis in dense cores can be a diagnostic of the importance of the magnetic field in environments of core formation. Theoretically, if the magnetic field is dominant, a dense core is expected to have its rotational axis aligned with it (Mouschovias & Paleologou 1979). Turbulent magnetohydrodynamic (MHD) simulations of core formation in converging flows also show that there are more dense cores with their rotational axes better aligned with the magnetic fields when initially the magnetic field is dominating over the turbulence in converging flows (Chen & Ostriker 2018). In addition, the alignment between the magnetic field and rotational axis can be an important parameter during the collapse of dense cores. MHD simulations show that when the magnetic field is misaligned with the rotational axis in a collapsing dense core, the efficiency of magnetic braking decreases, and more angular momentum can be transferred to the vicinity of the central protostar, resulting in the formation of a larger rotationally supported disk (Joos et al. 2012; Li et al. 2013; Hirano et al. 2020). Similar effects are also seen in MHD simulations with turbulence, where the local turbulence in a collapsing core can cause misalignment between the magnetic field and the rotational axis (e.g., Gray et al. 2018; Lam et al. 2019). Theoretically, an outflow is expected to launch along the rotational axis of a star–disk system (e.g., Blandford & Payne 1982; Pudritz & Norman 1983). The MHD simulations also show that in a collapsing dense core, the direction of the bipolar outflow on a scale of a few thousand astronomical units is along the rotational axis of the

dense core, even if this axis is initially misaligned with the magnetic field (Ciardi & Hennebelle 2010; Hirano et al. 2020). Thus, observationally, the direction of a bipolar outflow in a protostellar source can be a proxy for the rotational axis of its natal dense core, and statistical studies of the alignment between the magnetic fields and outflows in protostellar sources are crucial to better understand the formation of dense cores and circumstellar disks around protostars.

The alignment between the magnetic fields on the core scale of ~0.1 pc and outflows in low-mass protostars has been studied with a sample of seven sources using the SHARP polarimeter at the Caltech Submillimeter Observatory (Davidson et al. 2011; Chapman et al. 2013). On the assumption that the observed magnetic field structures trace an hourglass morphology, these single-dish studies suggest that the magnetic field tends to align with the outflow direction. In contrast, interferometric studies of ~20–30 low-mass protostars with the Combined Array for Research in Millimeter-wave Astronomy (CARMA) at spatial resolutions of ~1000 au show that the magnetic fields in the protostellar envelopes on a scale of a few thousand astronomical units are randomly oriented with respect to the outflow directions (Hull et al. 2013, 2014; Hull & Zhang 2019). Similar studies of 12 sources with the Submillimeter Array (SMA) suggest a bimodal distribution, where the magnetic fields in protostellar envelopes are either aligned with or perpendicular to the outflow directions (Galametz et al. 2018). The results obtained with these single-dish and interferometric observations seem to be inconsistent. However, the sample sizes of the previous single-dish studies are limited. On the other hand, in contrast with the single-dish observations, the magnetic field structures on the envelope scale observed with the interferometers are more likely to be affected by collapse and rotational motion in the protostellar envelopes, and possibly do not represent the initial configurations. Therefore, single-dish observations toward a large sample of protostars to probe their large-scale magnetic fields, which may still preserve the initial configurations, are needed to investigate the alignment between the magnetic field and rotational axis in dense cores.

The James Clerk Maxwell Telescope (JCMT) large program, B-fields In STar-forming Region Observations (BISTRO; Ward-Thompson et al. 2017), provides excellent data sets to study the magnetic field in star-forming regions. The BISTRO program observes polarized thermal continuum emission from dust at 850 μm and 450 μm using the polarimeter POL-2 (Friberg et al. 2016) for the bolometer SCUBA-2 (Holland et al. 2013). The first part of the survey, BISTRO-1, observed 16 fields in dense parts of the Gould Belt star-forming regions and covered a total area of >110 arcmin^2 with a total observing time of 224 hr. The BISTRO-1 observations have been completed. There are two

on-going follow-up BISTRO surveys, BISTRO-2 to continue the observations of the Gould Belt regions and to include other intermediate- and high-mass star-forming regions and BISTRO-3 to observe regions at different evolutionary stages and different spatial scales. Each follow-up survey also has a total observing time of 224 hr and targets 16 fields. A series of studies on the structures and strengths of the magnetic field and the properties of the dust grains in several star-forming regions have been conducted with the BISTRO program (Pattle et al. 2017, 2018, 2019; Kwon et al. 2018; Soam et al. 2018; Coudé et al. 2019; Liu et al. 2019; Wang et al. 2019a; Doi et al. 2020). In the present paper, we study the alignment between the magnetic fields and outflows in 62 low-mass protostars using BISTRO and archival POL-2 data, and discuss the observed distribution of the angles between the magnetic fields and the outflows in the context of the formation of dense cores and circumstellar disks.

2. Sample

Our sample sources were selected from dense molecular clouds in nearby low-mass star-forming regions at distances less than 450 pc observed by the JCMT BISTRO survey (program ID: M16AL004 and M17BL011), including Taurus, Perseus, Ophiuchus, and Serpens Main. A part of the BISTRO results of these regions has been published by Kwon et al. (2018), Soam et al. (2018), Coudé et al. (2019), Liu et al. (2019), Pattle et al. (2019), and Doi et al. (2020), and the remaining data of regions in Taurus and Serpens Main will be presented in detail in the forthcoming papers by C. Eswaraiah et al. (2020, in preparation), W. Kwon et al. (2020, in preparation), and Y.-W. Tang et al. (2020, in preparation). The Auriga star-forming region was also observed by the BISTRO survey (Ngoc et al. 2020). Since no young protostars are associated with clear bipolar outflows in the Auriga BISTRO field, these data are not included here. In addition, we searched the JCMT data archive for the POL-2 data of other nearby molecular clouds and Bok globules, and we retrieved the data taken with the regular projects M17AP067 (PI: P. Koch), M17AP073 (PI: W. Kwon), M17BP058 (PI: W. Kwon), and M17BP070 (PI: A. Soam). Some of these data have been published by Soam et al. (2019) and Yen et al. (2019). Then, from these star-forming regions, we selected low-mass Class 0 and I protostars whose molecular outflows have been imaged with interferometric observations at spatial resolutions of a few hundred astronomical units and show more or less well defined axes or cavity walls, so that the directions of their outflows could be accurately determined.[44] These selection criteria led to a sample of 62 Class 0 and I protostars. Table 1 lists all the sample sources with their outflow directions obtained from the literature and their basic properties. This represents the complete sample of young protostars that have been observed to host clear bipolar outflows in the BISTRO-1 survey fields of the low-mass star-forming regions. The distributions of the bolometric temperature (T_{bol}) and luminosity (L_{bol}) in our sample are presented in Figure 1. We note that there are more than a factor of two more Class 0 and I protostars in these star-forming regions than in those included here (Dunham et al. 2008; Enoch et al. 2008; Evans et al. 2009), but there are no suitable measurements of their outflow directions with interferometric observations of these additional sources. Thus, they are not included in this work.

3. POL-2 Data and Analysis

In this work, we used the POL-2 data at 850 μm. The angular resolution of the JCMT POL-2 observations at 850 μm is 14$\farcs$6, corresponding to spatial scales from 2000 to 6000 au at the distances to our sample protostars. We reduced all the POL-2 data with the software *Starlink* (Currie et al. 2014) and the task *pol2map* of the version updated on 2019 November 6. We followed the standard procedure of the data reduction as described in Pattle et al. (2017, 2019). The instrumental polarization model of "JAN2018" was adopted.[45] The data were first reduced with the default pixel size of 4$''$. Then every 3×3 pixels in the final Stokes IQU maps were binned to have a pixel size of 12$''$, which is comparable to the angular resolution, to extract polarization detections. Our detection criteria of the polarized emission are signal-to-noise ratios of Stokes I and polarized intensities both higher than three and polarization percentage lower than 20%, which is typically the maximum polarization percentage observed in star-forming regions by Planck (Planck Collaboration et al. 2015). Thus, the uncertainty in the polarization orientation of each detection is always ≲9°. The detected polarization orientations were rotated by 90° to infer the orientations of the magnetic field.

To measure the mean orientations of the magnetic fields in the dense cores or clumps[46] associated with the protostars in our sample, we first applied the two-dimensional version of the core/clump identification algorithm *Clumpfind* (Williams et al. 1994) on the Stokes I maps with a pixel size of 4$''$ and separated the molecular clouds into individual dense cores or clumps. The results are shown in Section 4 and Appendix A. Then, we calculated the mean Stokes Q and U of the polarization detections within the area of each dense core or clump identified by *Clumpfind*, and computed the mean magnetic field orientation from the mean Stokes Q and U. For the isolated dense cores in our sample–L1521F, L1527, HH 212, HH 111, and B335–we simply included all the polarization detections in the observed fields to compute their mean Stokes Q and U and the resulting mean magnetic field orientations. Although L1157 is also an isolated dense core, there is extended emission along the northwest–southeast direction detected by the JCMT POL-2 observations, and this extended component is likely related to the powerful outflow in L1157 (Bachiller et al. 2001; Tafalla et al. 2015) and is distinct from the central compact core (Figure 12). Thus, for L1157, we only used the detections within the central core identified by *Clumpfind* to compute its mean magnetic field orientation. The measured mean orientations of the magnetic field on a ~0.1 pc scale in all the protostars in our sample are listed in Table 1.

---

[44] We note that this selection criterion may bias our sample and exclude pole-on outflows. Nevertheless, we have tested this effect in our simulations of distributions of misalignment angles (Section 4.2) by excluding pairs of vectors with one of them aligned with the line of sight within a certain degree. We confirmed that the simulated distributions are not affected.

[45] The default instrumental polarization model used by *pol2map* was changed from "JAN2018" to "Aug2019" in 2020 April. The difference at 850 μm between the two models is expected to be less than the noise (https://www.eaobservatory.org/jcmt/2020/04/change-to-the-default-ip-model-used-by-pol2map/).

[46] Single-dish polarimetric observations of molecular clouds and Bok globules show that the polarized intensity generally increases with increasing Stokes I intensity, even though the polarization percentage decreases with it (e.g., Wolf et al. 2003; Coudé et al. 2019). Thus, the polarized emission is expected to be proportional to density and is more sensitive to dense regions along the line of sight.

Table 1
Sample List

| Name	Region	Distance (pc)	R.A. (J2000)	Decl. (J2000)	T_{bol} (K)	L_{bol} ($L_\odot$)	Outflow Orientation	Mean B Field Orientation	Reference
L1448 IRS 2	L1448	288	03:25:22.41	+30:45:13.3	43	3.6	118°	138° ± 2°	1, 2
L1448 IRS 2E	L1448	288	03:25:25.66	+30:44:56.7	15	0.05	165°	9° ± 2°	1, 2
L1448 IRS 3Bc[a]	L1448	288	03:25:35.67	+30:45:34.1	57	<8.3	128°	169° ± 1°	1, 2
L1448 IRS 3Ba[a,b]	L1448	288	03:25:36.38	+30:45:14.7	57	<8.3	122°	17° ± 3°	1, 2
L1448 IRS 3Bb[a,b]	L1448	288	03:25:36.50	+30:45:21.9	57	<8.3	38°	17° ± 3°	1, 2
L1448-mm[b]	L1448	288	03:25:38.88	+30:44:05.3	47	8.4	162°	21° ± 30°	1, 2
L1448C-S[b]	L1448	288	03:25:39.14	+30:43:57.9	163	0.68	43°	21° ± 30°	1, 2
Per-emb 17	L1455	279	03:27:39.10	+30:13:03.1	39	4.2	10°	65° ± 4°	1, 2
L1455 IRS 4	L1455	279	03:27:43.28	+30:12:28.8	65	1.4	115°	80° ± 3°	1, 2
Per-emb 3	NGC 1333	299	03:29:00.58	+31:12:00.2	32	0.5	96°	53° ± 6°	1, 2
NGC 13333 IRAS 4A	NGC 1333	299	03:29:10.54	+31:13:30.9	29	7	35°	60° ± 1°	1, 2
NGC 1333 IRAS 4B1[a,b]	NGC 1333	299	03:29:12.02	+31:13:08.0	28	<4	0°	71° ± 1°	1, 2
NGC 1333 IRAS 4B2[a,b]	NGC 1333	299	03:29:12.84	+31:13:06.9	28	<4	90°	71° ± 1°	1, 2
NGC 1333 IRAS 7[b]	NGC 1333	299	03:29:11.26	+31:18:31.1	59	2.8	150°	92° ± 1°	1, 2
Per-emb 21[b]	NGC 1333	299	03:29:10.67	+31:18:20.2	45	6.9	48°	92° ± °	1, 2
NGC 1333 IRAS 2A1[a,b]	NGC 1333	299	03:28:55.57	+31:14:37.0	69	<19	14°	79° ± 2°	1, 2
NGC 1333 IRAS 2A2[a,b]	NGC 1333	299	03:28:55.56	+31:14:36.4	69	<19	104°	79° ± 2°	1, 2
NGC 1333 IRAS 1a[a,b]	NGC 1333	299	03:28:37.09	+31:13:30.8	103	<9.1	123°	83° ± 8°	1, 2
NGC 1333 IRAS 1b[a,b]	NGC 1333	299	03:28:37.22	+31:13:31.8	103	<9.1	169°	83° ± 8°	1, 2
NGC 1333 IRAS 2B	NGC 1333	299	03:28:57.37	+31:14:15.8	106	5.3	24°	55° ± 4°	1, 2
SVS 13A[b]	NGC 1333	299	03:29:03.77	+31:16:03.8	188	32.5	130°	164° ± 1°	1, 2
RNO15-FIR[b]	NGC 1333	299	03:29:04.1	+31:14:46.2	36	0.4	145°	164° ± 1°	1, 2
Per-emb 37	NGC 1333	299	03:29:19.0	+31:23:14.3	22	0.5	37°	131° ± 3°	1, 2
Per-emb 49	NGC 1333	299	03:29:12.95	+31:18:14.3	239	1.1	25°	92° ± 1°	1, 2
Per-emb 50	NGC 1333	299	03:29:07.77	+31:21:57.1	128	23.2	104°	175° ± 1°	1, 2
Per-emb 58	NGC 1333	299	03:28:58.42	+31:22:17.5	322	0.63	167°	119° ± 2°	1, 2
SVS 13B[b]	NGC 1333	299	03:29:03.08	+31:15:51.7	20	1	160°	164° ± 1°	1, 2
SVS 13C[b]	NGC 1333	299	03:29:01.97	+31:15:38.1	21	1.5	8°	164° ± 1°	1, 2
Per-emb 6	Perseus B1	301	03:33:14.4	+31:07:10.9	52	0.3	60°	144° ± 2°	1, 2
Per-emb 10	Perseus B1	301	03:33:16.45	+31:06:52.5	30	0.6	51°	156° ± 1°	1, 2
B1-a	Perseus B1	301	03:33:16.66	+31:07:55.2	132	1.5	101°	146° ± 1°	1, 2
B1-c	Perseus B1	301	03:33:17.85	+31:09:32	48	3.7	131°	95° ± 1°	1, 2
B1-b[b]	Perseus B1	301	03:33:20.96	+31:07:23.8	157	0.17	30°	157° ± 1°	1, 2
B1-bN[b]	Perseus B1	301	03:33:21.21	+31:07:43.7	14	0.32	90°	157° ± 1°	1, 2
B1-bS[b]	Perseus B1	301	03:33:21.36	+31:07:26.4	17	0.70	112°	157° ± 1°	1, 2
HH 211-mms	IC 348	295	03:43:56.81	+32:00:50.2	27	1.8	116°	152° ± 1°	1, 2
IC 348 MMSa[a,b]	IC 348	295	03:43:57.07	+32:03:04.8	30	<1.5	167°	153° ± 2°	1, 2
IC 348 MMSb[a,b]	IC 348	295	03:43:57.69	+32:03:10.0	30	<1.5	36°	153° ± 2°	1, 2
Per-emb 16[b]	IC 348	295	03:43:50.98	+32:03:24.1	39	0.4	10°	113° ± 3°	1, 2
Per-emb 28[b]	IC 348	295	03:43:51.01	+32:03:08.0	45	0.7	112°	113° ± 3°	1, 2
Per-emb 62	IC 348	295	03:44:12.98	+32:01:35.4	378	1.8	24°	145° ± 9°	1, 2
IRAS 04169+2702	B211/B213	140	04:19:58.46	+27:09:56.9	133	0.77	64°	102° ± 6°	3, 4
IRAS 04166+2706	B211/B213	140	04:19:42.50	+27:13:36.0	139	0.3	30°	47° ± 3°	5, 6
L1521F	L1521F	140	04:28:38.9	+26:51:35.0	20	0.03	70°	21° ± 6°	7, 8
L1527	L1527	140	04:39:53.88	+26:03:09.7	44	1.9	92°	82° ± 11°	9, 10
HH 212	HH 212	414	05:43:51.41	−01:02:53.1	41	9	23°	35° ± 4°	11, 12
HH 111	HH 111	414	05:51:46.25	+02:48:29.7	69	20	97°	67° ± 2°	11, 13
GSS 30 IRS 3	Ophiuchus A	138	16:26:21.72	−24:22:50.9	86	33	20°	79° ± 1°	14, 15
VLA 1623A	Ophiuchus A	138	16:26:26.39	−24:24:30.7	10	1.10	125°	75° ± 1°	16, 17
Elias 32	Ophiuchus B	138	16:27:28.4	−24:27:21.7	321	5	91°	151° ± 3°	14, 18
Elias 33	Ophiuchus B	138	16:27:30.2	−24:27:43.9	460	12	129°	153° ± 2°	14, 18
S68N[b]	Serpens Main	436	18:29:48.09	+01:16:43.3	30	14	131°	85° ± 1°	19
S68Nc1[b]	Serpens Main	436	18:29:48.72	+01:16:55.6	<40	<2.1	109°	85° ± 1°	19
S68Nb1[b]	Serpens Main	436	18:29:49.51	+01:17:10.9	<60	<0.9	68°	85° ± 1°	19
Serpens SMM1b[a,b]	Serpens Main	436	18:29:49.67	+01:15:21.2	39	<109	165°	98° ± 1°	9, 20
Serpens SMM1a[a,b]	Serpens Main	436	18:29:49.8	+01:15:20.3	39	<109	135°	98° ± 1°	9, 20
Serpens SMM1d[a,b]	Serpens Main	436	18:29:49.99	+01:15:23.0	39	<109	80°	98° ± 1°	9, 20
Serpens SMM4B[a,b]	Serpens Main	436	18:29:56.53	+01:13:11.5	<30	<2.6	76°	48° ± 3°	19
Serpens SMM4A[a,b]	Serpens Main	436	18:29:56.72	+01:13:15.6	<30	<2.6	14°	48° ± 3°	19
Serpens SMM11[b]	Serpens Main	436	18:30:00.39	+01:11:44.6	<29	<0.9	76°	94° ± 1°	19

Table 1
(Continued)

Name	Region	Distance (pc)	R.A. (J2000)	Decl. (J2000)	T_{bol} (K)	L_{bol} ($L_\odot$)	Outflow Orientation	Mean B Field Orientation	Reference
B335	B335	165	19:37:00.90	+07:34:09.5	36	1.4	99°	111° ± 2°	9, 10
L1157	L1157	352	20:39:06.27	+68:02:15.7	42	7	163°	159° ± 1°	21, 22

Notes. The outflow orientations and the mean magnetic field orientations on 0.05–0.5 pc scales are presented as position angles increasing from north to east. Typically, the uncertainties in the outflow orientations are ∼10° (Stephens et al. 2017). The uncertainties in the mean magnetic field orientations are calculated with the error propagation of the uncertainties of the individual polarization detections. If the blue- and redshifted lobes of a bipolar outflow are not symmetric, we adopt the position angle of the mean axis of the two lobes as the outflow orientation. For each protostar, the first reference is for the bolometric temperature (T_{bol}) and luminosity (L_{bol}), and the second is for the outflow orientation. For HH 212 and HH 111, L_{bol} is from the second reference. If only one reference is listed, both T_{bol} and outflow orientation are from that reference. The distances to Perseus, Ophiuchus, and Serpens are adopted from Ortiz-León et al. (2018a, 2018b), the distance to Orion from Menten et al. (2007), the distance to Taurus and Cepheus from Torres et al. (2009) and Zucker et al. (2019), and the distance to B335 from Watson (2020).
[a] This source is in a multiple system, where individual protostars are not resolved in infrared observations. Thus, the same T_{bol} and L_{bol} are assigned to it and its companions. The assigned L_{bol} is the total luminosity of the system and should be considered as an upper limit for the individual sources.
[b] In this source, there are multiple sample protostars in the same dense core or clump.
References. (1) Tobin et al. (2016) and references therein; (2) Stephens et al. (2017); (3) Young et al. (2003); (4) Takakuwa et al. (2018); (5) Chen et al. (1995); (6) Wang et al. (2019b); (7) Hsieh et al. (2017); (8) Takahashi et al. (2013); (9) Kristensen et al. (2012); (10) Hull et al. (2014); (11) Tafalla et al. (2013); (12) Lee et al. (2017b); (13) Lee et al. (2016); (14) van Kempen et al. (2009); (15) Friesen et al. (2018); (16) Murillo et al. (2013); (17) Santangelo et al. (2015); (18) Kamazaki et al. (2019); (19) Aso et al. (2019); (20) Tychoniec et al. (2019); (21) Motte & André (2001); (22) Maury et al. (2019).
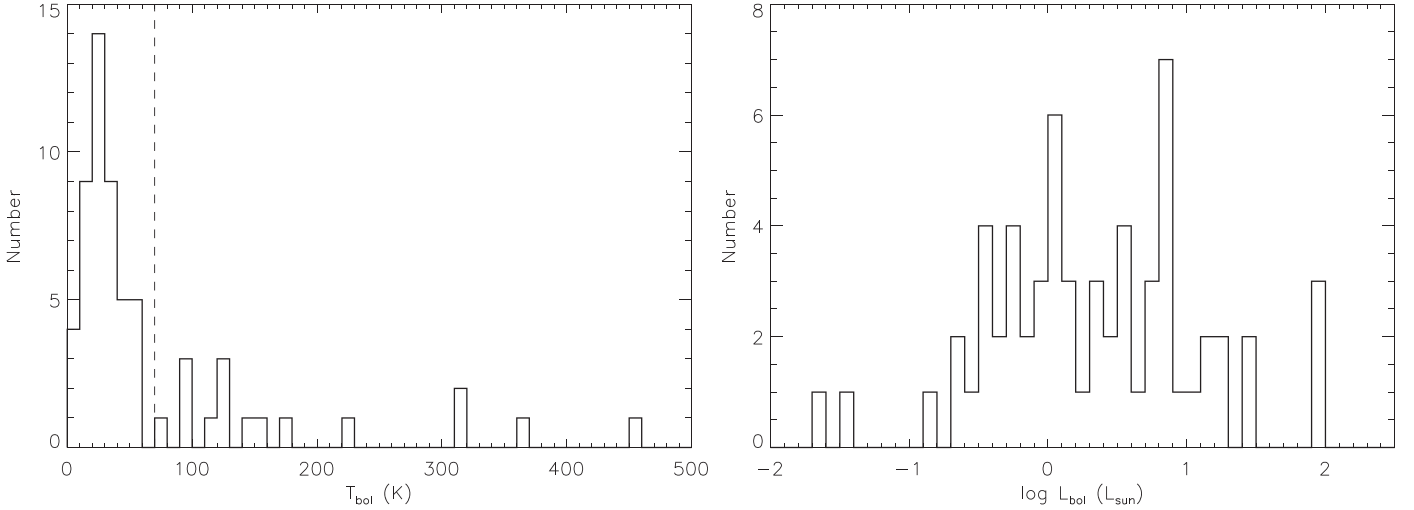
Figure 1. Distributions of bolometric temperature (T_{bol}; left) and luminosity (L_{bol}; right) in our sample. A vertical dashed line denotes T_{bol} of 70 K. If T_{bol} and L_{bol} of a sample source only have upper limits, the upper limits are plotted. Details are given in Table 1.

In our calculations of the mean magnetic field orientations, each polarization detection was weighted equally. We have also computed the mean orientations by weighting the individual detections with their polarized intensities or signal-to-noise ratios. The differences between the mean orientations calculated with the different weightings are typically less than 5°, and are less than 9° in all the sources, except for L1448 mm and L1448C-S, where the differences are 19°. The mean magnetic field orientations in L1448 mm and L1448C-S also have larger uncertainties (30°) than all the other sources. The comparisons of the mean magnetic field orientations computed with different weightings are listed in Appendix B. The computed mean orientation is not sensitive to the exact area or boundary of a dense core identified by *Clumpfind*, as discussed below. In addition, we note that in some dense cores or clumps there could be multiple protostars, which could have different outflow directions. In this case, we consider all the protostars in this dense core or clump to have the same mean magnetic field orientation, but we report different degrees of misalignment

between their outflows and the mean magnetic field. They are considered as independent measurements in the following analysis.

4. Results

4.1. Magnetic Structures in Example Sources

Figure 2 presents the results of our core/clump identification in the Perseus B1 region as an example. The contours delineate the area of the dense cores or clumps associated with our sample protostars identified by *Clumpfind*. The locations of the sample protostars and their outflow directions are also plotted. The results of the core/clump identification for the remaining sample protostars are shown in Appendix A. The detected magnetic field orientations in individual dense cores and clumps associated with our sample protostars are shown in Figures 3 and 4 and Appendix C. In most of the dense cores and clumps on scales of 0.05–0.5 pc in our sample, the magnetic fields tend to show uniform structures, so representative mean orientations can be
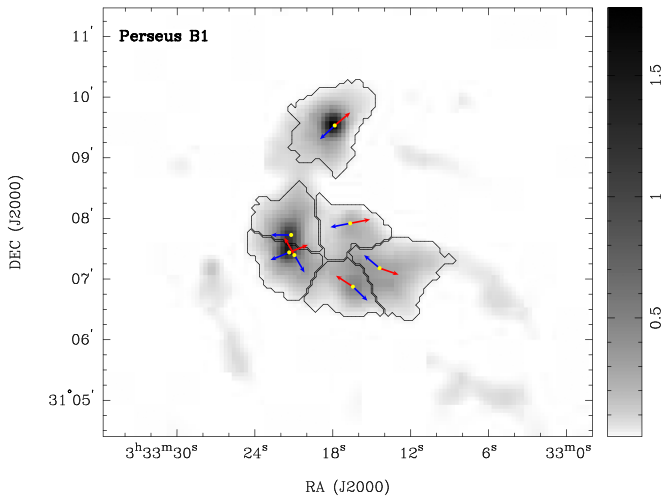
Figure 2. Stokes *I* intensity map (gray scale; in units of Jy beam^{-1}) obtained with the JCMT POL-2 observations and the results of the core/clump identification using *Clumpfind* in the Perseus B1 region. Contours delineate the area of identified dense cores or clumps associated with our sample protostars. Yellow dots show the locations of our sample protostars, and blue and red arrows represent the orientations of their blue- and redshifted outflow lobes.

derived. Figure 3 shows the maps of the detected magnetic field segments in B1-a, NGC 1333 IRAS 4B, and NGC 1333 IRAS 7 as examples. The distributions of the magnetic field orientations inferred from the individual polarization detections in these protostellar sources are clustered and peak close to the derived mean orientations of the magnetic fields in their dense cores (middle panels). In addition, there is no significant dependence of the magnetic field orientations on the radial distances of the individual detections from the positions of the protostars (right panels). Thus, our results show that the magnetic field orientations do not change significantly as a function of position within these dense cores, although there are a few sources showing broader distributions of the magnetic field orientations in the dense cores, such as L1448 IRS 3Ba,b, L1448-mm (L1448C-S), HH 211-mms, L1527, and Serpens SMM4A (Appendix C).

We note that in a few sources, the magnetic field orientations at larger distances of >6000–10,000 au from the protostars are different from those closer to them. In Figure 4, we present the results for GSS 30 IRS 3, B1-bN, and VLA 1623A as examples. In GSS 30 IRS 3, the magnetic field segments at distances larger than 6000 au show different orientations from those at smaller distances, but the number of these segments is relatively small. As a result, the mean magnetic field orientation in GSS 30 IRS 3 is not affected by those detections at larger distances. The other source, B1-bN, shows a similar trend in which the magnetic field orientations change by ~40° at distances larger than 10,000 au, and those polarization detections at the larger distances also do not affect the computed mean orientation significantly. VLA 1623A is an extreme case in our sample. The magnetic field orientations in VLA 1623A clearly change as a function of distance to the protostar. In VLA 1623A, the magnetic field close to the protostar within a radius of 6000 au is more misaligned with the outflow, and the magnetic field becomes more aligned with the outflow as the distance to the protostar increases. Nevertheless, the number of sample sources showing clear distance dependence is small (<5) compared with the total sample size (Appendix C). We have confirmed that only including the polarization detections at distances less than 6000 au or 10,000 au from the protostars has

little impact on the final statistics, and does not affect our discussions and conclusions.

### 4.2. Distribution of the Misalignments

We computed the misalignment angle between the outflow orientation and the mean orientation of the magnetic field in the dense core or clump for each sample protostar. The misalignment angle is defined to be between 0° and 90°. Figure 5 presents the distribution of the misalignment angles, where the bin size is 10°. The distribution peaks at misalignment angles between 15° and 35°, and there are fewer protostars with their magnetic fields perfectly aligned with or perpendicular to the outflows. The fraction of our sample sources having misalignment angles larger than 45° is 40% (25/62) and that larger than 70° is 13% (8/62). To investigate whether there is any potential bias in our results due to source properties and spatial resolutions, we compared the misalignment angles with the sizes, total fluxes, mean intensities, and mean polarization percentages of the dense cores as well as the distances to the sources, and found there is no dependence of the misalignment angles on these parameters (Appendix D).

Due to projection effects, two misaligned vectors in three-dimensional (3D) space have a higher probability of appearing more aligned on the plane of the sky. Thus, to study the intrinsic distribution of the misalignment in 3D space, we generated mock samples of pairs of vectors assuming different probability distributions of the 3D misalignment. Then, we randomly defined a line-of-sight direction and projected these pairs of vectors on the assumed plane of the sky to compare with the observations. We assumed three different probability distributions of the 3D misalignment: (1) two vectors are randomly oriented with respect to each other, (2) the misalignment between two vectors has uniform probability from 0° to 90°, and (3) the probability distribution of the misalignment is a Gaussian function. The probability distributions of the 3D misalignment for these scenarios are shown in Figure 6(a). In the case of two randomly oriented vectors, there is a higher probability of having an orthogonal configuration in 3D space. Figure 6(b) presents the cumulative distributions of the 3D misalignment. Then we projected these distributions onto the plane of the sky (Figure 6(c)).

If two vectors are randomly oriented with respect to each other in 3D space (red dashed curves in Figure 6), the distribution of the projected misalignment angles is flat (when projected onto the plane of the sky), which is different from the observed distribution. We performed a Kolmogorov–Smirnov (K-S) test on these mock and observed samples. The probability that the two are drawn from the same distribution is 20%. For the mock sample with a uniform probability distribution of the 3D misalignment (blue dotted curves in Figure 6), after the projection, the distribution of the misalignment is not uniform, and there are more sources showing smaller misalignment angles. The K-S test on these mock and observed samples suggests that the probability that the two are drawn from the same distribution is <1%. For the mock samples with the Gaussian probability distribution of the 3D misalignment, we generated several different samples by varying the center θ_c and dispersion δ_θ of the Gaussian probability distributions. Then, we projected these distributions of the 3D misalignments and performed the K-S tests. We found that the probability of the mock and observed samples being drawn from the same distribution is higher than 90% when θ_c is close to 50° and δ_θ is close to 15° (green dashed–dotted curves in Figure 6).
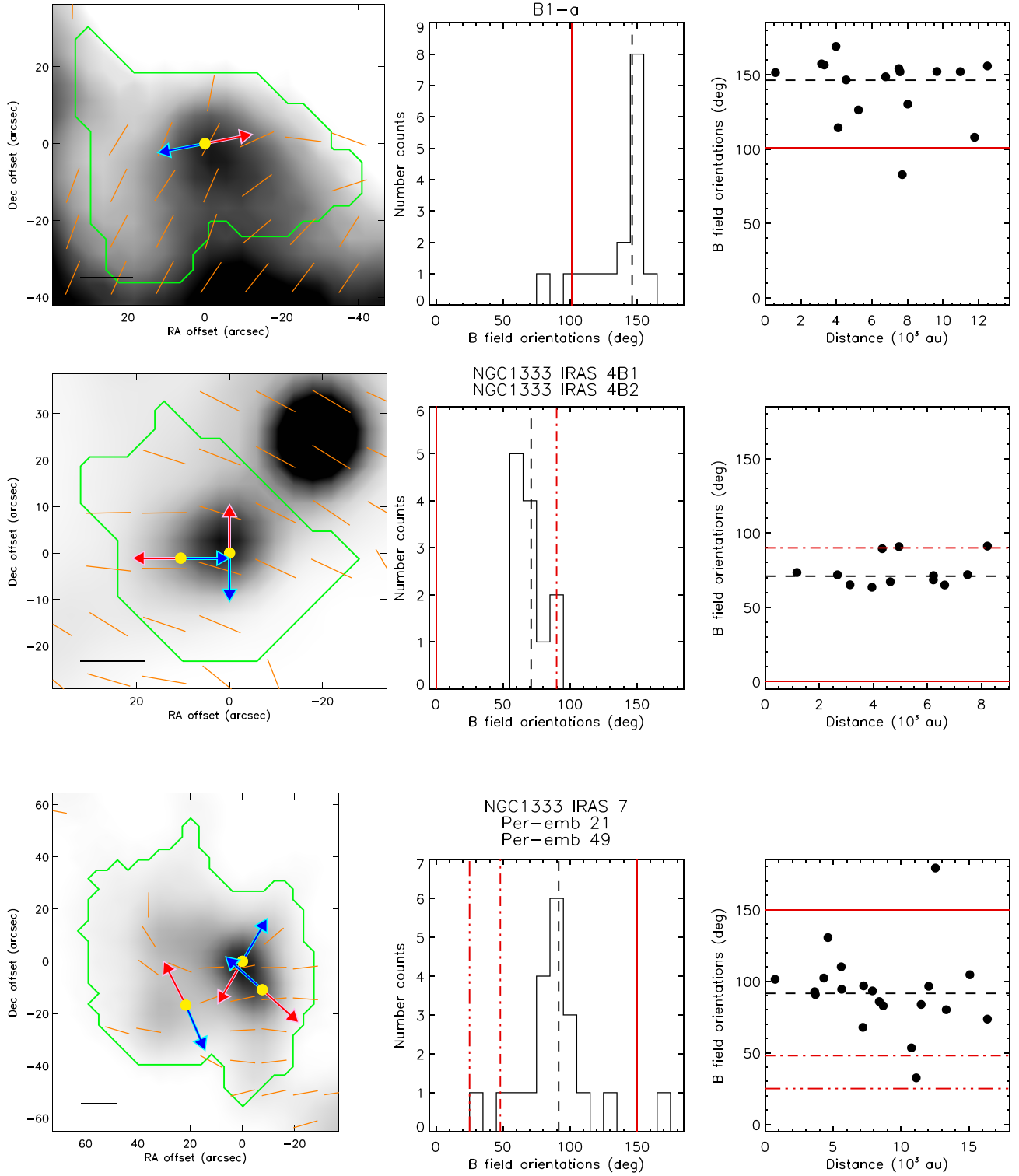
Figure 3. Magnetic field orientations in B1-a (upper row), NGC 1333 IRAS 4B (middle row), and NGC 1333 IRAS 7 (lower row; including Per-emb 21 and 49) observed by JCMT POL-2. B1-a is located in the Perseus B1 region (Figure 2). NGC 1333 IRAS 4B and NGC 1333 IRAS 7 are located in the NGC 1333 region in Perseus (Figure 10). Left panels show the Stokes *I* maps (gray scale) of the dense cores, where the sample protostars are embedded, and green contours delineate the area of the dense cores identified by *Clumpfind*. Yellow dots show the locations of the protostars, and blue and red arrows represent the orientations of their blue- and redshifted outflows. Black horizontal segments denote the spatial scale of 0.02 pc (or ~4000 au). Middle panels present the distributions of the position angles of the individual magnetic field orientations detected with the JCMT POL-2 observations. Right panels present the distributions of the position angles of the magnetic field orientations as a function of distance from the protostars. If multiple protostars are present in one core, the distances between the magnetic field orientations and the protostar closest to the Stokes *I* intensity peak are calculated. In the middle and right panels, black dashed lines denote the mean magnetic field orientations computed from the averaged Stokes *Q* and *U* emission in the area of the dense cores, and red solid and dashed–dotted (if there are multiple outflows) lines show the position angles of the outflows. The names of the protostars are labeled in the order from western to eastern sources above the middle panel in each row.
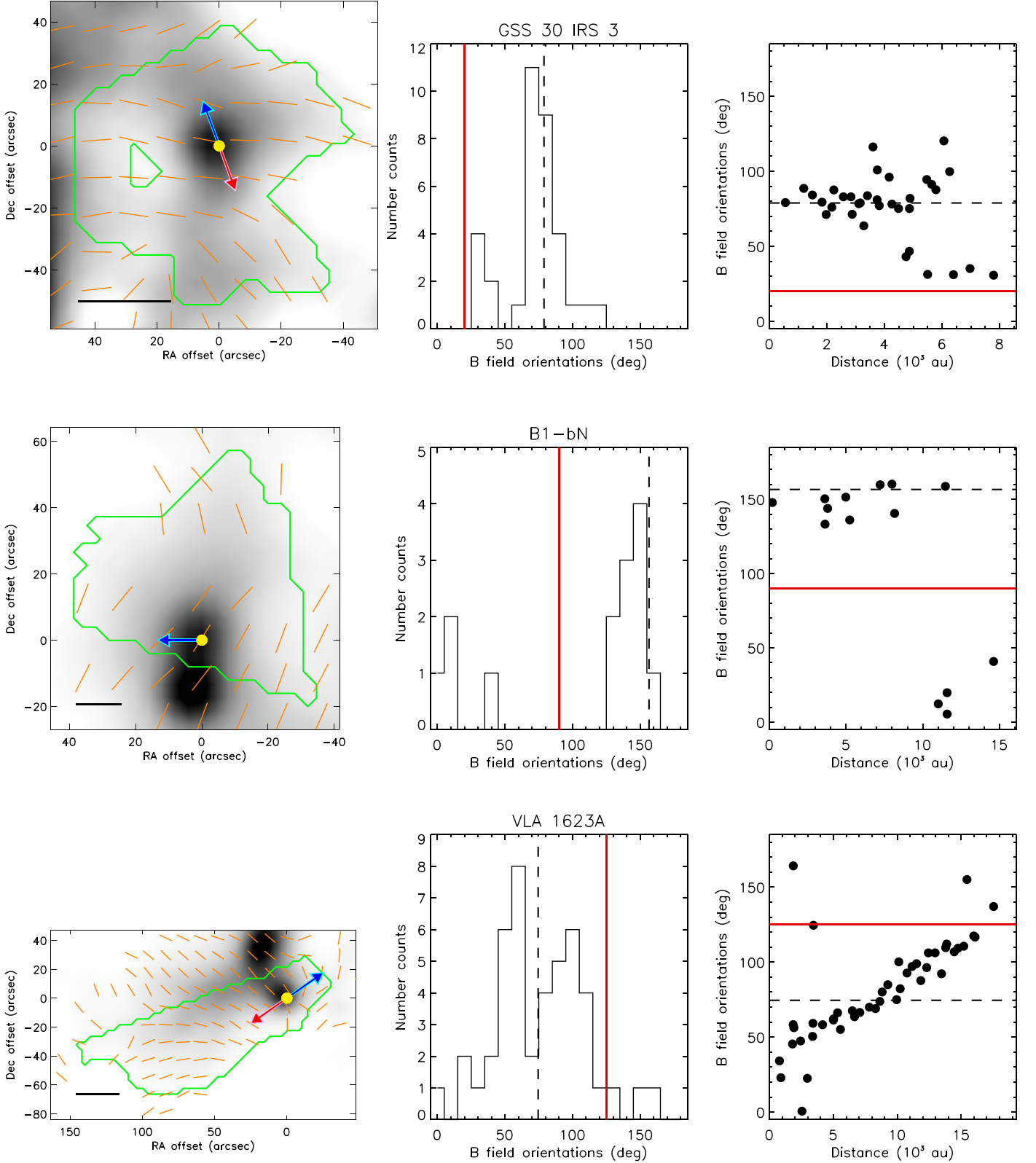
Figure 4. Same as Figure 3, but for GSS 30 IRS 3 (top row), B1-bN (middle row), and VLA 1623A (bottom row).

Therefore, our results show that the 3D misalignment angles between the outflows and magnetic fields in our sample sources are not uniformly distributed. Our results could suggest that the outflows tend to be misaligned with the mean magnetic field orientations in the associated dense cores or clumps by $50° \pm 15°$

and are less likely randomly oriented with respect to the magnetic fields in 3D space. Nevertheless, our results do not rule out the possibility of random orientations of the outflows and the magnetic fields. A similar trend that outflows may have preferred orientations with respect to the magnetic fields has also been
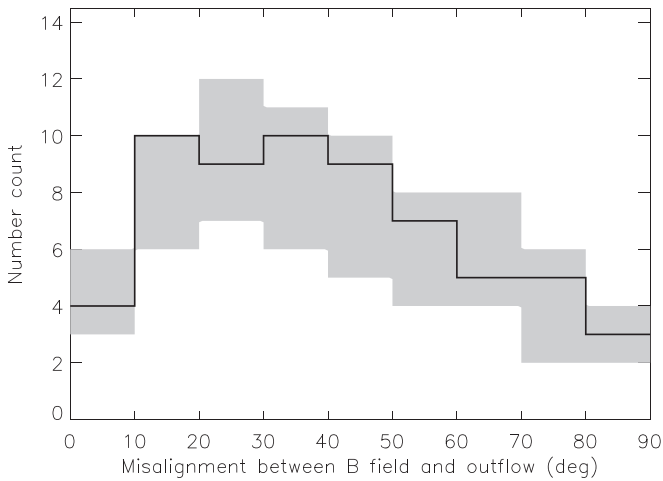
Figure 5. Distribution of the misalignment angles between the outflow orientations and the mean magnetic field orientations in the dense cores and clumps (thick step curve). The gray area represents the 1σ uncertainty of the distribution, assuming that there is a $10°$ uncertainty in each measurement of the misalignment. We note that the total number count is conserved when interpreting the uncertainty of the distribution. If the number count in one bin decreases, the number counts in nearby bins increase.

suggested in the high-mass star-forming region W43-MM1 (Arce et al. 2020), although the possibility of random orientations of outflows and magnetic fields is also not ruled out in that study.

4.3. Dependence of the Misalignments on T_{bol} and Spatial Scale

Figure 7(a) compares the misalignment angles with the bolometric temperatures (T_{bol}) of our sample protostars. T_{bol} can be an evolutionary indicator (e.g., Chen et al. 1995), although it also depends on the inclination and structures of the central disk and inner envelope in a protostellar source (Young & Evans 2005; Crapsi et al. 2008). Our results show that there is no clear dependence of the misalignment on the evolution as measured by T_{bol}. For any given range of T_{bol}, there is a wide range of misalignment angles. The correlation coefficient between T_{bol} and the misalignment angles is computed to be 0.1. Nevertheless, we note that the Class 0 and I sources may have different distributions of the misalignments. The misalignment angles in the Class I sources are clustered in a smaller range from $20°$ to $60°$ (Figure 7(b)). However, in our sample, the number of Class I sources is smaller than the number of Class 0 sources by a factor of three. A more uniform sample is needed to examine any possible difference in the distributions of the misalignments between the Class 0 and I sources.

We also compared the misalignments on small and large scales (Figure 8). For each protostar, we computed the small-scale misalignment from the single polarization detection closest to the position of the protostar. Considering the resolution of the JCMT POL-2 observations of $14''$, the magnetic field orientation inferred from the detection closest to the protostar could represent the averaged magnetic field structure in the protostellar envelopes on a scale of 1000–3000 au at the distances to our sample protostars. This spatial scale is also comparable to those probed by interferometric polarimetric observations with CARMA and SMA (e.g., Hull et al. 2013, 2014; Galametz et al. 2018). As shown in previous studies that compare single-dish and interferometric results (e.g., Hull et al. 2014; Yen et al. 2019; Doi et al. 2020), single-dish measurements at stellar positions can generally

present the mean orientations of magnetic field on small scales observed by interferometers. In 17 of our sample sources, the mean magnetic field orientations on a 1000 au scale were also measured with the CARMA, SMA, and/or Atacama Large Millimeter/submillimeter Array (ALMA) observations (Hull et al. 2014; Galametz et al. 2018; Sadavoy et al. 2019). We compared our JCMT POL-2 and those interferometric results. Our measured small-scale misalignments are indeed correlated with the interferometric measurements (Appendix E).

In Figure 8, most of the data points are scattered around the diagonal dashed line, suggesting that in most cases the difference in the magnetic field orientations on the large and small scales is approximately $10°–20°$ or less. The orientations of the large- and small-scale magnetic fields in 48% (30/62) of the sample sources are consistent within $10°$, and those in 78% (47/62) within $20°$. The comparison between the large-scale misalignments observed by JCMT and the small-scale misalignments observed by the interferometers also shows the same trend as above, i.e., that the difference between large- and small-scale magnetic fields is mostly $10°–20°$ (Appendix E). In addition, in Figure 8 there are several data points distributed in the upper left half of the plot, but only a few in the lower right half. In 11 (18%) of our sample protostars, the misalignment angles on the small scale are more than $20°$ larger than those on the large scale, and only four protostars (6%) show the opposite. Thus, our results also suggest that the degrees of misalignment on the small scale tend to remain the same or become larger than those on the large scale in our sample.

5. Discussion

5.1. Comparison with Interferometric Results

The CARMA observations of $\sim$20–30 low-mass protostars show that the magnetic fields in the protostellar envelopes on a scale of a few hundred to a few thousand astronomical units are randomly oriented with respect to the outflows (Hull et al. 2013, 2014). The SMA observations of 12 protostars suggested a bimodal distribution of the misalignment angles, where the magnetic fields in protostellar envelopes are either aligned with or perpendicular to the outflows (Galametz et al. 2018). Our JCMT POL-2 results show a number distribution of the misalignment angles different from the random or bimodal distributions. In these JCMT POL-2 data of 62 protostars, more than half of the sample sources have their magnetic fields misaligned with the outflows by $15°–45°$ on the plane of the sky. The different number distributions of misalignment found by the JCMT POL-2 and interferometric observations could be due to the different spatial scales probed by these observations. The large-scale magnetic fields observed with JCMT might have still preserved the initial morphologies. On the other hand, as the infalling and rotational velocities increase with decreasing radii in the protostellar sources, the small-scale magnetic fields could be shaped by the gas motions, as suggested by the interferometric studies (Hull et al. 2014; Galametz et al. 2018). In addition, several interferometric observations at high angular resolutions, which well resolved the magnetic field structures in the protostellar envelopes on a scale of hundreds of astronomical units, revealed tangled, pinched, and/or wrapped magnetic fields (Girart et al. 2006; Stephens et al. 2013; Rao et al. 2014; Hull et al. 2017, 2017, 2020; Cox et al. 2018; Maury et al. 2018; Sadavoy et al. 2018, 2019; Kwon et al. 2019; Le Gouellec et al. 2019; Lee et al. 2019; Yen et al. 2019, 2020; Ko et al. 2020). Our JCMT POL-2 results also show that in 11 of our sample
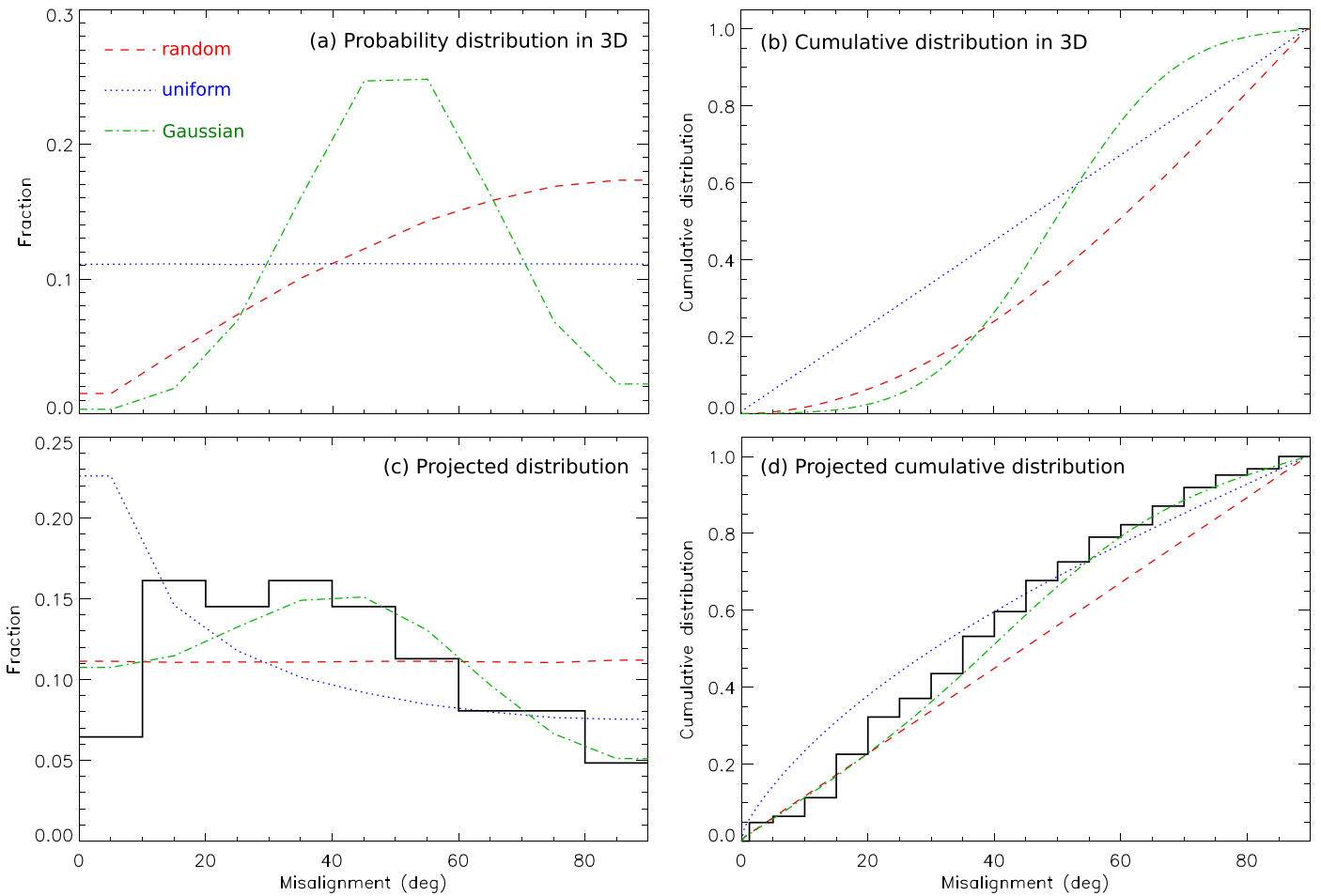
Figure 6. (a) Distributions of the misalignment angles in 3D space in our mock samples. (b) Cumulative distributions of the 3D misalignment angles in our mock samples. (c) Distributions of the misalignment angles projected onto the plane of the sky in our mock samples in comparison with the observed distribution. (d) Cumulative distributions of the projected misalignment angles in our mock samples in comparison with the observations. Blue dotted and green dashed–dotted curves show the cases where the probability distribution of the 3D misalignment is uniform and a Gaussian function, respectively. This Gaussian function has a center at 50° and a 1σ dispersion of 15°. Red dashed curves show the case where two vectors are randomly oriented with respect to each other in 3D space. The observed distributions are shown by solid black step curves. The bin size in (a) and (c) is 10°. The step size of the observed cumulative distribution in (d) is 5°.

sources the magnetic field orientations inferred from the detections closest to the protostars are more misaligned with the outflows than the magnetic field measured on larger scales, and there are only four sources showing the opposite trend. These results demonstrate the changes in the magnetic field structures from the large to small scales, which are possibly due to the dynamics of collapsing and rotating dense cores.

5.2. Implications for Core Formation

Given the assumption that the outflow directions trace the directions of the angular momenta of the dense cores in our sample sources[47] (e.g., Blandford & Payne 1982; Pudritz & Norman 1983; Ciardi & Hennebelle 2010; Hirano et al. 2020), our JCMT POL-2 results could suggest that the angular momenta of the dense cores tend to be misaligned with the magnetic fields by 50° ± 15° if the distribution of the angles between the magnetic fields and the outflows in 3D space is a

Gaussian function, although we do not rule out the possibility that the outflows are randomly oriented with respect to the magnetic fields (Section 4.2). In addition, several dense cores in our sample harbor multiple protostars with their outflows oriented in different directions, which could hint at nonuniform rotation in these dense cores. In the classical picture of core formation without consideration of turbulence, the angular momentum is expected to align with the magnetic field because the efficiency of magnetic braking is higher when the angular momentum and the magnetic field are perpendicular (e.g., Mouschovias & Paleologou 1979). Our results do not support this classical picture.

Properties of the magnetic field and angular momentum of dense cores formed in magnetized and turbulent molecular clouds have been often studied with numerical simulations (e.g., Burkert & Bodenheimer 2000; Gammie et al. 2003; Li et al. 2004; Dib et al. 2010; Chen & Ostriker 2014, 2015; Lee et al. 2017a; Kuznetsova et al. 2020). Chen & Ostriker (2018) compared the distributions of the misalignment between the angular momenta and the magnetic fields in the dense cores formed in their 3D turbulent MHD simulations of converging flows with different degrees of the magnetization and turbulence. Their simulations can be roughly classified into three groups: dominant magnetic field (M5 and B20), dominant

---

[47] We note that in numerical simulations with turbulence, rotation in dense cores could be nonuniform (e.g., Dib et al. 2010; Zhang et al. 2018; Verliat et al. 2020). In this case, the outflow direction may not represent the direction of the net angular momentum of an entire dense core but is related to the angular momentum of the material that has been accreted to form the central star–disk system.
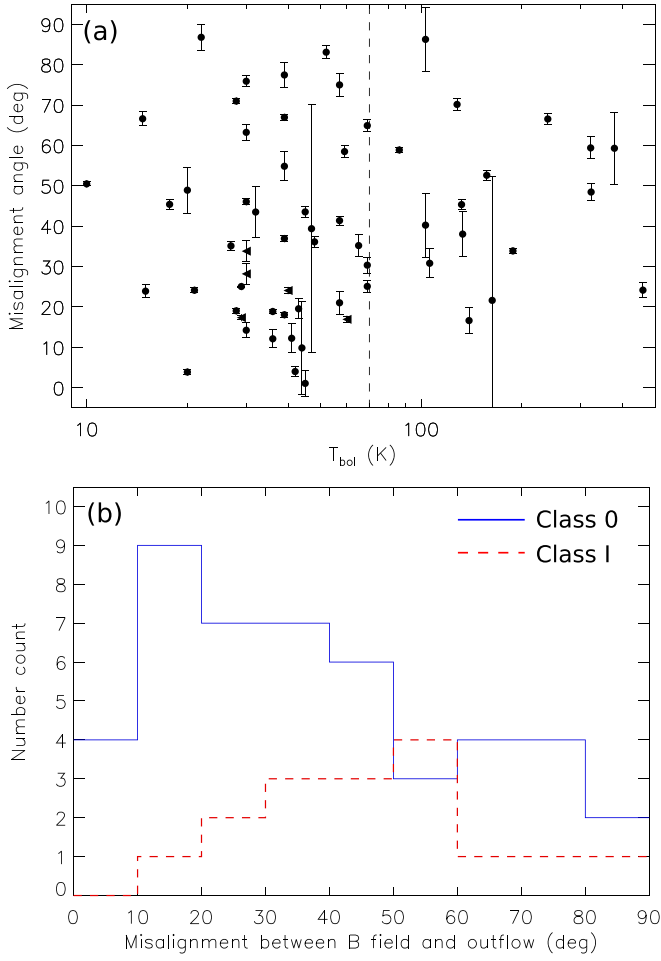
Figure 7. (a) Angles between the outflow orientations and the mean orientations of the large-scale magnetic field in the dense cores and clumps as a function of bolometric temperature (T_{bol}) of our sample protostars. A vertical dashed line denotes T_{bol} of 70 K, which has been adopted to classify Class 0 and I protostars (Chen et al. 1995). Error bars represent the uncertainties in the mean magnetic field orientations from the error propagation of the uncertainties of the individual polarization detections. For several sources, the error bars are smaller than the symbol size. There is an additional uncertainty in the misalignment angles due to the uncertainty in the outflow orientations, which is typically 10°. If T_{bol} of a protostar in our sample only has an upper limit (Table 1), then that upper limit is plotted as a left-facing triangle. (b) Distributions of the misalignment angles of the Class 0 (blue step curve) and I (red dashed step curve) protostars in our sample.

Figure 8. Comparison of the misalignment between the outflows and the magnetic field orientations on two different scales. The vertical axis shows the angles between the outflows and the small-scale (1000–3000 au) magnetic fields, and the horizontal axis shows the angles between the outflows and the large-scale (0.05–0.5 pc or 10^4–10^5 au) magnetic fields. Two dotted lines denote a difference in angle of $\pm20°$. Horizontal error bars represent the uncertainties in the mean magnetic field orientations from the error propagation of the uncertainties of the individual polarization detections. For several sources, the horizontal error bars are smaller than the symbol size. Vertical error bars are the uncertainties in the polarization angles of the detections closest to the protostars.

turbulence (B5 and M20), and moderate magnetic field and turbulence (M10B10), where the labels in the parentheses are those adopted in Chen & Ostriker (2018) to represent different simulations. Figure 9(a) presents the distributions of the 3D misalignment angles between the magnetic fields and the angular momenta in the dense cores in these simulations. In the simulations, the dense cores may not have uniform rotation and magnetic field structures. These misalignment angles are the angles between the mean magnetic field orientations and directions of the net angular momentum of the simulated dense cores. In the simulations with dominant turbulence (B5 and M20), the distributions peak at large misalignment angles of 50°–70°. In contrast, the simulations with the dominant magnetic field (M5 and B20) show flatter distributions of the misalignment angles without a dominant peak. The distribution of the misalignment angles in the simulation with the moderate magnetic field and turbulence (M10B10) follows this trend. It

has a peak at a misalignment angle of 30° on top of a flat distribution. As pointed out by Chen & Ostriker (2018), the misalignment angle between the magnetic field and the angular momentum tends to increase as turbulence becomes more dominant. This trend is also seen in other simulations (e.g., Joos et al. 2013). Our observational results suggest that the distribution of the misalignment between the magnetic fields and the outflows on a 0.05–0.5 pc scale is not flat (Figure 6). This is different from the distributions in the simulations with dominant magnetic field (B20 and M5). In addition, our observational results could suggest a predominantly large number of protostars with their magnetic fields misaligned with the outflows by $50° \pm 15°$ on a 0.05–0.5 pc scale. This observed distribution is more similar to those from the simulations M10B10 and B5, which also peak at misalignment angles of 30°–60°, but differs from that of the simulation with the strongest turbulence (M20). In the most turbulent simulation (M20), there is a larger fraction of cores ($\sim$45%) with misalignment angles larger than 60° compared to the observations ($\sim$25%). Therefore, the comparison between our observational results and these numerical simulations suggests that the magnetic field is unlikely dominant during the core formation, and our results also hint at significant turbulence in the environment where these dense cores form.

The distributions presented in Figure 9(a) are the misalignment angles measured in 3D space. To make a more direct comparison with the observational data, we projected these angles on an assumed plane of the sky, similar to the analysis in Section 4.2. We repeated this process 50,000 times. Each time we randomly selected a direction of the line of sight, and computed the number distributions of the projected misalignment angles. All the misalignment angles of individual dense cores in the simulations were treated independently, and we did
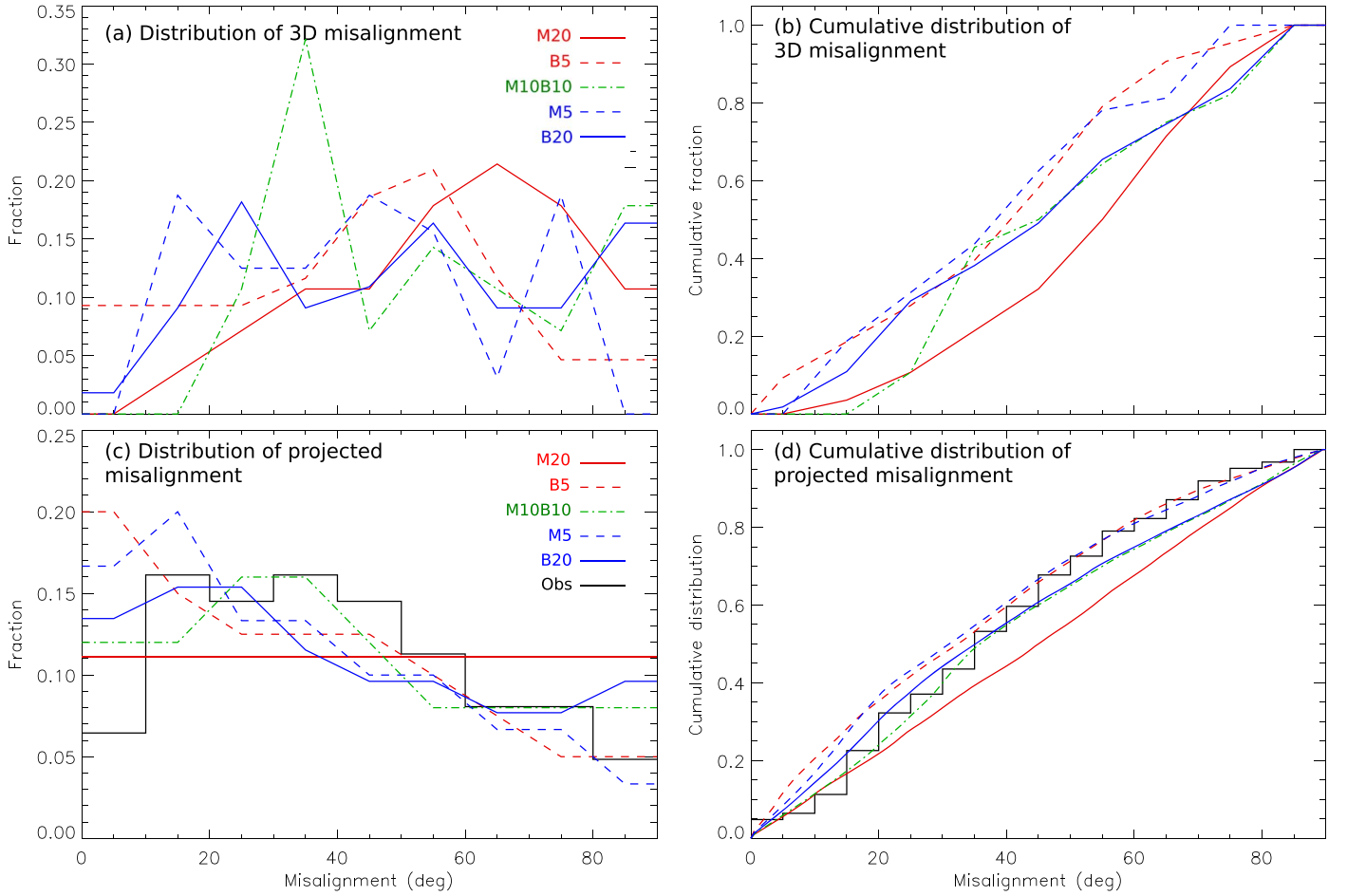
Figure 9. (a) Distributions and (b) cumulative distributions of the misalignment angles between the magnetic fields and the angular momenta in the simulated dense cores in 3D space (Chen & Ostriker 2018). Different lines with different colors show the distributions from different simulations (see Section 5.2). Red solid and dashed lines represent the simulations with dominant turbulence, and blue solid and dashed lines the simulations with dominant magnetic field. The green dashed–dotted line represents the simulation with moderate magnetic field and turbulence. (c) and (d) are the same as (a) and (b) but after projecting the misalignment angles onto the plane of the sky. In (c) and (d), the black step curves show the observed distributions of the misalignment angles in our sample sources. The bin size in (a) and (c) is 10°. The step size of the observed cumulative distribution in (d) is 5°.

not consider any possible correlations between the directions of the magnetic fields or angular momenta of different cores, although they formed in the same molecular clouds. Nevertheless, this simplification is appropriate because our sample protostars are located in several different molecular clouds. Finally, we computed number counts for different misalignment angles from these 50,000 iterations. The distributions of the misalignment angles of these simulated dense cores projected onto the plane of the sky are plotted in Figure 9(c), and the cumulative distributions are plotted in Figure 9(d).

The most turbulent simulation (M20), which has a distribution of the 3D misalignment skewed toward larger angles, shows a flat distribution after the projection, and this is different from the observed distribution (Figure 9(c)). In contrast, the simulations with dominant magnetic field (M5 and B20), which have flatter distributions of the 3D misalignment angles, show distributions of the misalignment skewed toward smaller angles and peaking at <20° after the projection. The simulation B5, where turbulence dominates over the magnetic field, also shows a similar distribution after the projection, because there is a significant fraction of dense cores with well aligned magnetic fields and angular momenta in this simulation (Figure 9(a)). Compared to the observations, these three simulations have more sources showing projected misalignment angles smaller than 20°. Among these five simulations, the

distribution of the projected misalignment angles from M10B10 is the one most similar to that observed. The K-S test suggests a probability of 85% that the observed distribution and the distribution in M10B10 are drawn from the same distribution, while for all the other models, the possibilities are below 30% (27% for B20, 3% for M5, 2% for B5, and 16% for M20). Nevertheless, we note that the numbers of dense cores in these simulations (55 in B20, 32 in M5, 43 in B5, and 28 in M20 and M10B10) may not be large enough to unveil underlying distributions of the misalignment in the simulated environments. Therefore, this comparison with the simulations only qualitatively demonstrates that to reproduce the observed distribution of the misalignment, there are likely only a few protostellar sources having very small or large misalignment angles, and a dominant fraction of sources have intermediate misalignment angles, like ~30° in the case of M10B10. Overall, the observed distribution is more like the one in the simulation with the moderate magnetic field and turbulence (M10B10), and deviates more from those from the simulations with a dominant magnetic field or dominant turbulence (B20, M5, B5, and M20), but we do not rule out the scenarios of dominant magnetic field or turbulence in the environments of core formation from the comparison with these simulations.

5.3. Implication for Disk Formation

Ideal MHD simulations of a nonturbulent, rotating, and collapsing dense core with its magnetic field aligned with the rotational axis show that magnetic braking is very efficient to transfer the angular momentum of collapsing material outward and suppress the formation of a Keplerian disk larger than 10 au around the central protostar (e.g., Allen et al. 2003; Mellon & Li 2008). This is the so-called "magnetic-braking catastrophe". Misalignment between the magnetic field and rotational axis in a dense core has been proposed to be a mechanism to reduce the efficiency of magnetic braking and to enable formation of a large Keplerian disk with a size of tens of astronomical units (e.g., Joos et al. 2012; Krumholz et al. 2013).

Keplerian disks with sizes larger than tens of astronomical units have often been observed around protostars (Williams & Cieza 2011). In the ALMA survey of the Lupus star-forming regions (Ansdell et al. 2018), 95 Class II sources were observed, 71 of them were detected in the 1.3 mm continuum, and 32 disks were resolved in the continuum. The resolutions of these observations are 0″.2–0″.3, corresponding to ∼40 au, so these observations are able to resolve Keplerian disks with sizes of tens of astronomical units. The line emission in the disks in a subset of the Lupus sample is bright, and the Keplerian rotation is indeed detected (e.g., Ansdell et al. 2018; Yen et al. 2018). Thus, the fraction of resolved Keplerian disks in the Lupus star-forming regions is 34% (32/95) of the full sample and 45% (32/71) of the detected sources. Similar surveys have also been conducted toward the ρ Ophiuchus star-forming regions at similar spatial resolutions of ∼30 au (Cieza et al. 2019; Williams et al. 2019). Cieza et al. (2019) presented observational results for 21 Class I protostars, 41 protostars with flat spectra, and 120 Class II protostars. The disks around 12, 16, and 31 of these Class I, flat-spectrum, and Class II protostars were resolved in the 1.3 mm continuum, corresponding to fractions of resolved Keplerian disks of 57%, 39%, and 26%, respectively. In the Orion star-forming regions, an ALMA survey found that 36% (153/421) of the Class 0, I, and flat-spectrum protostars have disk radii larger than 50 au in the continuum emission (46% for Class 0, 38% for Class I, and 27% for flat-spectrum; Tobin et al. 2020). Therefore, these ALMA surveys suggest that the fractions of large Keplerian disks with sizes larger than 30–50 au around Class 0–II protostars range from approximately 30% to 60%.

These fractions should be considered as lower limits. This is because these are shallow surveys with integration times of one or a few minutes per source, and hence faint large disks and large disks with steep intensity profiles may not be detected or resolved. In addition, the disk radii tend to be larger in the line emission than in the continuum (Ansdell et al. 2018; Yen et al. 2018), but these shallow surveys are not sensitive enough to detect line emission in most of the targeted disks. We note that here we only consider large disks with sizes of tens of astronomical units, and the fraction of protostars surrounded by a disk is much higher (e.g., Haisch et al. 2001; Williams & Cieza 2011). Whether the mechanism of the misalignment is able to explain the observed numbers of large Keplerian disks has been discussed in the literature assuming random alignment between the magnetic field and the rotational axis in the natal dense cores (see, e.g., Krumholz et al. 2013; Li et al. 2013). Here we revisit this question with our new constraint on the distribution of the misalignment angles and the observed

number fractions of large Keplerian disks from the recent ALMA surveys.

The effects of the misalignment between the magnetic field and the rotational axis on disk formation have been studied with numerical simulations with ideal MHD conditions (Joos et al. 2012; Li et al. 2013), which exclude other possible mechanisms to reduce the efficiency of magnetic braking. These simulations show that when the median observed strength of the magnetic field of a mass-to-flux ratio[48] of two to three is adopted (Crutcher 2012), large Keplerian disks with sizes of tens of astronomical units only form if the initial magnetic field is almost perpendicular to the rotational axis. Our observational results show that fewer than 5% of protostars have projected misalignment angles larger than 80°. Even if we consider projection effects, based on our inferred Gaussian distributions of the 3D misalignment angles or the distribution in the numerical simulations M10B10 (the one most similar to our observational results; Section 5.2), the fractions of protostars having misalignment angles larger than 80° are estimated to be lower than 10%–20% (Figure 9). These numbers are approximately two to three times smaller than the lower limits of the observed fractions of large Keplerian disks with sizes larger than 30–50 au. We note that these MHD simulations may not be able to resolve formation of small Keplerian disks with sizes of ≲10 au. In our discussion of the observed fractions of the Keplerian disks, we only considered large Keplerian disks with sizes of tens of astronomical units. Therefore, with the typical mass-to-flux ratio of two to three, the misalignment between the magnetic field and the rotational axis of a dense core cannot be the primary mechanism to enable the formation of a large Keplerian disk.

On the other hand, Crutcher et al. (2010) suggest that the probability distribution of the mass-to-flux ratios in dense cores could be uniform with a minimum ratio of one. Joos et al. (2012) show that if the initial mass-to-flux ratios are larger than five, large Keplerian disks form when the misalignment angles are larger than 70°, and if the initial mass-to-flux ratios are larger than 17, large Keplerian disks always form regardless of the misalignment angles. Simulations with different initial density and velocity distributions by Li et al. (2013) show that large Keplerian disks form when the initial mass-to-flux ratios are larger than 10 and the misalignment angles are larger than 45°. Following discussions in Krumholz et al. (2013), we estimate the expected number fraction of large Keplerian disks (f_{disk}) as

$$f_{disk} = f_\lambda(5-10) \times f_{ang}(>70°)$$
$$+ f_\lambda(10-17) \times f_{ang}(>45°) + f_\lambda(>17), \quad (1)$$

where $f_\lambda(5-10)$, $f_\lambda(10-17)$, and $f_\lambda(>17)$ are the fractions of sources having mass-to-flux ratios of 5–10, 10–17, and >17, respectively, and $f_{ang}(>70°)$ and $f_{ang}(>45°)$ are the fractions of sources having misalignment angles larger than 70° and 45°, respectively. With a uniform distribution of the mass-to-flux ratio and our observed distributions of misalignment angles, the expected number fraction of large Keplerian disks is estimated to be ∼10%, which is more than a factor of three lower than the observed number fraction. If we also consider the parameters of mass-to-flux ratios of 3–5 and misalignment angles of 20°–45°

---

[48] Mass-to-flux ratio is defined as $\frac{\Phi}{2\pi\sqrt{G}}$, where Φ is the magnetic flux and G is the gravitational constant (Nakano & Nakamura 1978).

that form sub-Keplerian disks with flat rotational profiles, which are supported by both rotation and magnetic pressure, in the MHD simulations by Joos et al. (2012), the expected number fraction increases to ~20%, but this fraction is still lower than the observed value. These estimated expected number fractions are similar to the minimal possibility estimated by Krumholz et al. (2013), but are lower than their maximum possibility because Krumholz et al. (2013) include the parameters with which the simulations form sub-Keplerian disks or no disks in their estimation. On the other hand, observationally, large disks around protostars are often found to be Keplerian (e.g., Piétu et al. 2007; Simon et al. 2017). Thus, those cases of sub-Keplerian disks in the simulations may not represent observed disks. In addition, our observed distribution of the misalignment suggests a lower fraction of sources with large misalignments compared to the random distribution.

In summary, the numerical simulations suggest that in the limit of ideal MHD, the mass-to-flux ratio needs to be larger than 5–10 together with a misalignment angle between the magnetic field and the rotational axis larger than 45° to form a Keplerian disk with a size of tens of astronomical units (Joos et al. 2012; Li et al. 2013). Observationally, the fraction of protostars having misalignment angles larger than 45° is likely ~50% (Section 4), and the probability of a dense core with a mass-to-flux ratio larger than 5–10 is 10%–20% (Crutcher et al. 2010). Therefore, with the misalignment alone, the expected fraction of large Keplerian disks with sizes of tens of astronomical units would be <10%–20%, a factor of two to three lower than the lower limits estimated from the observations. The combination of the observations and the MHD simulations suggests that the misalignment is unlikely a dominant mechanism to reduce the efficiency of magnetic braking and to enable formation of the large number of observed Keplerian disks with sizes larger than 30–50 au. Nevertheless, our results do not exclude the possibility that the misalignment could still reduce the efficiency of magnetic braking and prompt disk formation in individual sources, such as the case in HH 211 (Lee et al. 2019), but the number of sources with sufficiently large misalignment angles to have significant effects is small in our sample. In contrast, protostellar sources with well aligned magnetic fields and outflows can also exhibit significant rotational motion on a 1000 au scale, such as L1448 IRS 2 (Yen et al. 2015; Kwon et al. 2019; Gaudel et al. 2020). Thus, overall, the misalignment is unlikely a primary mechanism, and other mechanisms, such as nonideal MHD effects, could play a more important role in disk formation and growth (Tsukamoto et al. 2017; Zhao et al. 2016, 2018; Masson et al. 2016; Matsumoto et al. 2017; Lam et al. 2019; Wurster et al. 2019; Wurster & Bate 2019).

6. Summary

We measured the mean orientations of the magnetic fields in the dense cores on scales of 0.05–0.5 pc associated with 62 Class 0 and I protostars using the JCMT BISTRO-1 and archival POL-2 data. We compared the mean magnetic field orientations with the orientations of the outflows launched from those protostars. The main results are summarized below.

1. The observed distribution of the misalignment between the magnetic field and the outflow on the plane of the sky is not flat, but rather peaks at 15°–35°. There are 23% (14/62) of the sample sources having the misalignment on the plane of the sky smaller than 20° and only 13% (8/62) larger than 70°. We have compared the measured misalignment angles with the sizes, total fluxes, mean intensities, and mean polarization percentages of the sample dense cores and clumps as well as the distances to the sample sources. The measured misalignment angles do not depend on these source properties and the spatial resolutions. Thus, we expect that there is no bias in the observed distribution of the misalignment introduced by the source properties or the nonuniform spatial resolutions in the sample.

2. After considering projection effects, the K-S test suggests that the observed distribution of the misalignment is different from a uniform distribution, and is also less likely (20% probability) a random distribution of outflow and magnetic field orientations. If the distribution of the misalignment in 3D space is assumed to be a Gaussian function, the K-S tests suggest that the probability of most (68%) of the sample sources having misalignment angles of $50° \pm 15°$ between the magnetic field and the outflow in the 3D space is higher than 90%.

3. There is no significant correlation between the misalignment angles and bolometric temperatures of the protostars. For any given range of the bolometric temperatures, there is a wide range of the misalignment between the magnetic fields and the outflows in our sample. Thus, there is no clear sign of time evolution of the misalignment angles.

4. The observed distribution of the misalignment is different from the results obtained with the CARMA and SMA observations, which suggest random or bimodal distributions of the misalignment. The difference is most likely due to different spatial scales probed by the JCMT POL-2 and interferometric observations. The magnetic field on a 0.05–0.5 pc scale observed with the JCMT might have preserved the initial morphology, while the magnetic field in the protostellar envelopes on scales from hundreds to thousands of astronomical units observed with the interferometers can be already shaped by the infalling and rotational motions in the envelopes. As a matter of fact, the JCMT POL-2 observations, when limited to the vicinity of the protostar, show that the magnetic field orientations become more misaligned with the outflows than the large-scale magnetic field in several sample sources. Thus, these results suggest changes in the magnetic field structures from the dense cores to the inner protostellar envelopes.

5. Given the assumption that the directions of the outflows trace the directions of the angular momenta of the dense cores in our sample sources, we compared the observed distribution of the misalignment with the turbulent MHD simulations of core formation in converging flows. The observed distribution is more similar to that in the simulations with moderate turbulence and magnetic field, where there are more dense cores with misalignment angles of 30°–40° between the magnetic field and the rotational axis. The simulations with a dominant magnetic field show flat distributions of the misalignment angles between the magnetic fields and rotational axes of dense cores, while the most turbulent simulation has a

high fraction (>45%) of cores having misalignment angles larger than 60°. The distributions of the misalignments in these simulations are different from our observational results. Therefore, our results could suggest that in the environment of the core formation, the energy density in the magnetic field is comparable to that in the turbulent velocity field of the gas, but the comparisons with these simulations do not have sufficient statistical significance to rule out the scenarios of dominant magnetic field or turbulence.

6. Misalignment between the magnetic field and rotational axis in a dense core has been proposed to be a mechanism to reduce the efficiency of magnetic braking and enable the formation of a large Keplerian disk with a size of tens of astronomical units around a protostar. MHD simulations show that when the mass-to-flux ratio is larger than 5–10 and the misalignment angle between the magnetic field and rotational axis is larger than 45° in a dense core, a large Keplerian disk with a size of tens of astronomical units can form even in the ideal MHD limit. Based on our observed distribution of the misalignment between the magnetic field and rotational axis in our sample and the assumption of a uniform probability distribution of the mass-to-flux ratios, the expected number fraction of protostars surrounded by a large Keplerian disk with a size of tens of astronomical units is <10%–20%. This is a factor of two to three lower than the number fractions (>30%–60%) of large disks with sizes larger than 30–50 au around protostars in nearby star-forming regions observed with the recent ALMA surveys. Consequently, our results suggest that the misalignment is not the primary mechanism to reduce the efficiency of magnetic braking and to enable formation of the observed number of large Keplerian disks with sizes larger than 30–50 au.

Appendix A
Identification of Core and Clumps

Figure 10 presents the Stokes *I* maps and the area of individual cores and clumps identified using *Clumpfind*.
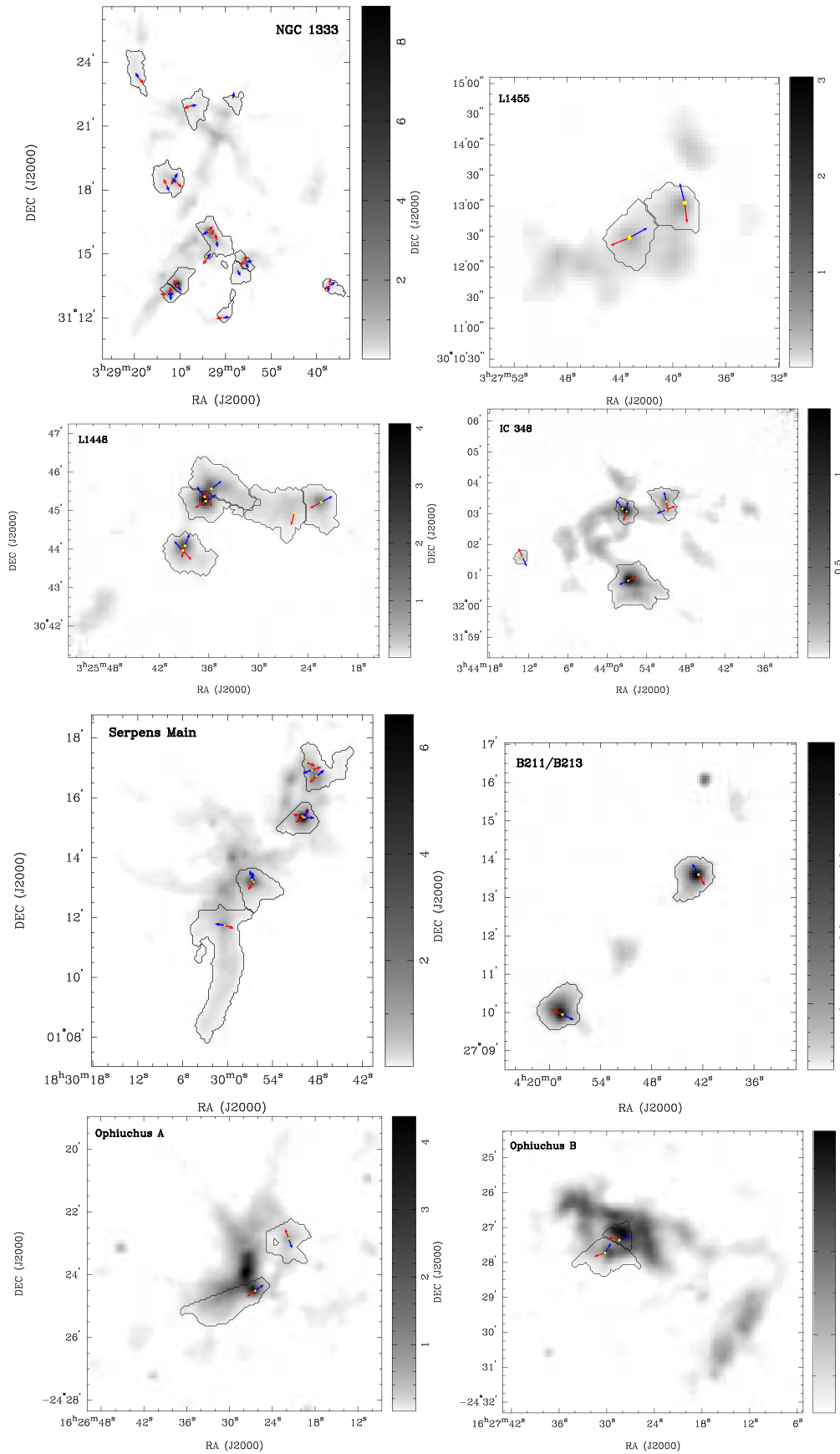
Figure 10. Same as Figure 2, but for the remaining regions in our sample. The name of the region is labeled in the upper right or left corner in each panel.

Appendix B
Mean Magnetic Field Orientations

Table 2 shows the mean magnetic field orientations computed without weighting and by weighting the individual polarization detections with their polarized intensities, signal-to-noise ratios, and Stokes I intensities. The differences between the mean orientations computed without weighting and with weighting by the polarized intensity and the signal-to-noise ratio are typically less than 5°, and are less than 9° in all the sources, except for L1448 mm and L1448C-S. The mean orientations computed with weighting by the Stokes I intensity tend to show larger differences. This is because the dense cores typically exhibit high intensity contrast between the center and outer regions, and the resultant mean orientations are more biased by the central detections when the weighting by the Stokes I intensity is applied.

Table 2
Sample List

Name	$\bar{B}_{\theta,\mathrm{nw}}$	$\bar{B}_{\theta,PI}$	$\bar{B}_{\theta,\mathrm{SN}}$	$\bar{B}_{\theta,I}$
L1448 IRS 2	138° ± 2°	136° ± 2°	137° ± 2°	129° ± 2°
L1448 IRS 2E	9° ± 2°	10° ± 2°	8° ± 2°	8° ± 2°
L1448 IRS 3Bc	169° ± 1°	168° ± 1°	168° ± 1°	167° ± 2°
L1448 IRS 3Ba	17° ± 3°	26° ± 3°	19° ± 3°	37° ± 3°
L1448 IRS 3Bb	17° ± 3°	26° ± 3°	19° ± 3°	37° ± 3°
L1448-mm	21° ± 31°	40° ± 17°	30° ± 30°	47° ± 16°
L1448C-S	21° ± 31°	40° ± 17°	30° ± 30°	47° ± 16°
Per-emb 17	65° ± 4°	64° ± 4°	64° ± 4°	70° ± 5°
L1455 IRS 4	80° ± 3°	81° ± 3°	75° ± 3°	84° ± 3°
Per-emb 3	53° ± 6°	55° ± 6°	55° ± 6°	53° ± 6°
NGC 1333 IRAS 4A	60° ± 1°	60° ± 1°	60° ± 1°	60° ± 1°
NGC 1333 IRAS 4B1	71° ± 1°	68° ± 1°	67° ± 1°	70° ± 1°
NGC 1333 IRAS 4B2	71° ± 1°	68° ± 1°	67° ± 1°	70° ± 1°
NGC 1333 IRAS 7	92° ± 1°	93° ± 1°	93° ± 1°	95° ± 1°
Per-emb 21	92° ± 1°	93° ± 1°	93° ± 1°	95° ± 1°
NGC 1333 IRAS 2A1	79° ± 2°	74° ± 1°	74° ± 1°	74° ± 1°
NGC 1333 IRAS 2A2	79° ± 2°	74° ± 1°	74° ± 1°	74° ± 1°
NGC 1333 IRAS 1a	83° ± 8°	79° ± 8°	81° ± 8°	84° ± 5°
NGC 1333 IRAS 1b	83° ± 8°	79° ± 8°	81° ± 8°	84° ± 5°
NGC 1333 IRAS 2B	55° ± 4°	57° ± 4°	58° ± 4°	69° ± 3°
SVS 13A	164° ± 1°	163° ± 1°	163° ± 1°	163° ± 1°
RNO15-FIR	164° ± 1°	163° ± 1°	163° ± 1°	163° ± 1°
Per-emb 37	131° ± 3°	132° ± 3°	131° ± 3°	127° ± 4°
Per-emb 49	92° ± 1°	93° ± 1°	93° ± 1°	95° ± 1°
Per-emb 50	175° ± 1°	174° ± 1°	174° ± 1°	171° ± 1°
Per-emb 58	119° ± 2°	117° ± 2°	117° ± 2°	120° ± 2°
SVS13B	164° ± 1°	163° ± 1°	163° ± 1°	163° ± 1°
SVS 13C	164° ± 1°	163° ± 1°	163° ± 1°	163° ± 1°
Per-emb 6	144° ± 2°	143° ± 2°	143° ± 2°	147° ± 2°

Table 2
(Continued)

| Name	$\bar{B}_{\theta,\mathrm{nw}}$	$\bar{B}_{\theta,PI}$	$\bar{B}_{\theta,\mathrm{SN}}$	$\bar{B}_{\theta,I}$
Per-emb 10	156° ± 1°	153° ± 1°	153° ± 1°	153° ± 1°
B1-a	146° ± 1°	148° ± 1°	147° ± 1°	146° ± 1°
B1-c	95° ± 1°	100° ± 1°	101° ± 1°	100° ± 1°
B1-b	157° ± 1°	157° ± 1°	156° ± 1°	153° ± 2°
B1-bN	157° ± 2°	155° ± 1°	155° ± 1°	149° ± 2°
B1-bS	157° ± 1°	157° ± 1°	156° ± 1°	153° ± 2°
HH 211-mms	152° ± 1°	155° ± 1°	156° ± 1°	154° ± 1°
IC 348 MMSa	153° ± 2°	153° ± 2°	152° ± 2°	154° ± 2°
IC 348 MMSb	153° ± 2°	153° ± 2°	152° ± 2°	154° ± 2°
Per-emb 16	113° ± 3°	113° ± 3°	113° ± 3°	113° ± 4°
Per-emb 28	113° ± 3°	113° ± 3°	113° ± 3°	113° ± 4°
Per-emb 62	145° ± 9°	145° ± 8°	145° ± 9°	145° ± 9°
IRAS 04169+2702	102° ± 6°	104° ± 4°	104° ± 5°	104° ± 5°
IRAS 04166+2706	47° ± 3°	47° ± 3°	47° ± 3°	47° ± 4°
L1521F	21° ± 6°	19° ± 5°	18° ± 5°	26° ± 5°
L1527	82° ± 12°	81° ± 10°	83° ± 10°	40° ± 6°
HH 212	35° ± 4°	34° ± 3°	32° ± 4°	35° ± 3°
HH 111	67° ± 2°	66° ± 2°	65° ± 2°	62° ± 2°
GSS 30IRS3	79° ± 1°	80° ± 1°	80° ± 1°	80° ± 1°
VLA 1623A	75° ± 1°	70° ± 1°	71° ± 1°	60° ± 1°
Elias 32	151° ± 3°	145° ± 2°	142° ± 2°	154° ± 3°
Elias 33	153° ± 2°	152° ± 2°	151° ± 2°	151° ± 1°
S68N	85° ± 1°	83° ± 1°	83° ± 1°	83° ± 1°
S68Nc1	85° ± 1°	83° ± 1°	83° ± 1°	83° ± 1°
S68Nb1	85° ± 1°	83° ± 1°	83° ± 1°	83° ± 1°
Serpens SMM1b	98° ± 1°	100° ± 1°	98° ± 1°	114° ± 1°
Serpens SMM1a	98° ± 1°	100° ± 1°	98° ± 1°	114° ± 1°
Serpens SMM1d	98° ± 1°	100° ± 1°	98° ± 1°	114° ± 1°
Serpens SMM4B	48° ± 3°	41° ± 2°	39° ± 2°	51° ± 3°
Serpens SMM4A	48° ± 3°	41° ± 2°	39° ± 2°	51° ± 3°
Serpens SMM11	94° ± 1°	94° ± 1°	93° ± 1°	94° ± 1°
B335	111° ± 2°	110° ± 2°	111° ± 2°	104° ± 3°
L1157	159° ± 1°	157° ± 1°	156° ± 1°	157° ± 1°

Note. $\bar{B}_{\theta,\mathrm{nw}}$, $\bar{B}_{\theta,PI}$, $\bar{B}_{\theta,\mathrm{SN}}$, and $\bar{B}_{\theta,I}$ are the mean magnetic field orientations of the dense cores or clumps computed from the mean Stokes Q and U without any weighting and with weighting by the polarized intensity, signal-to-noise ratio, and Stokes I intensity of the individual polarization detections, respectively. The uncertainties in the mean magnetic field orientations are calculated with the error propagation of the uncertainties of the individual polarization detections.

Appendix C
Number and Radial Distributions of Magnetic Field Orientations

Figures 11 and 12 present close-ups of the Stokes I maps, number distributions of the detected magnetic field orientations, and their radial dependences for all the sample sources expect for those presented in Figures 3 and 4.
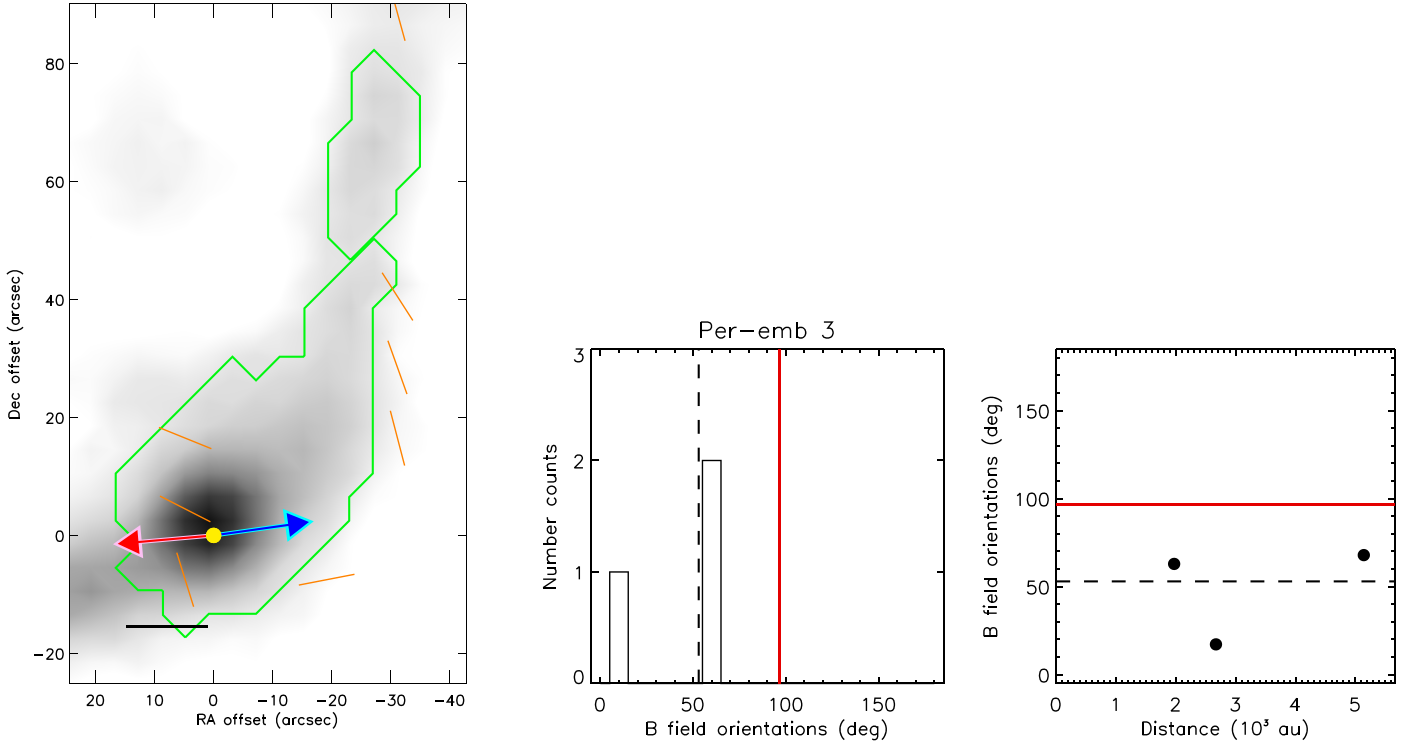
Figure 11. Same as Figures 3 and 4, but for the remaining sample sources. The source name is labeled above the middle panel of each row. Black horizontal segments denote the spatial scale of 0.02 pc (or ∼4000 au).

(The complete figure set (22 images) is available.)
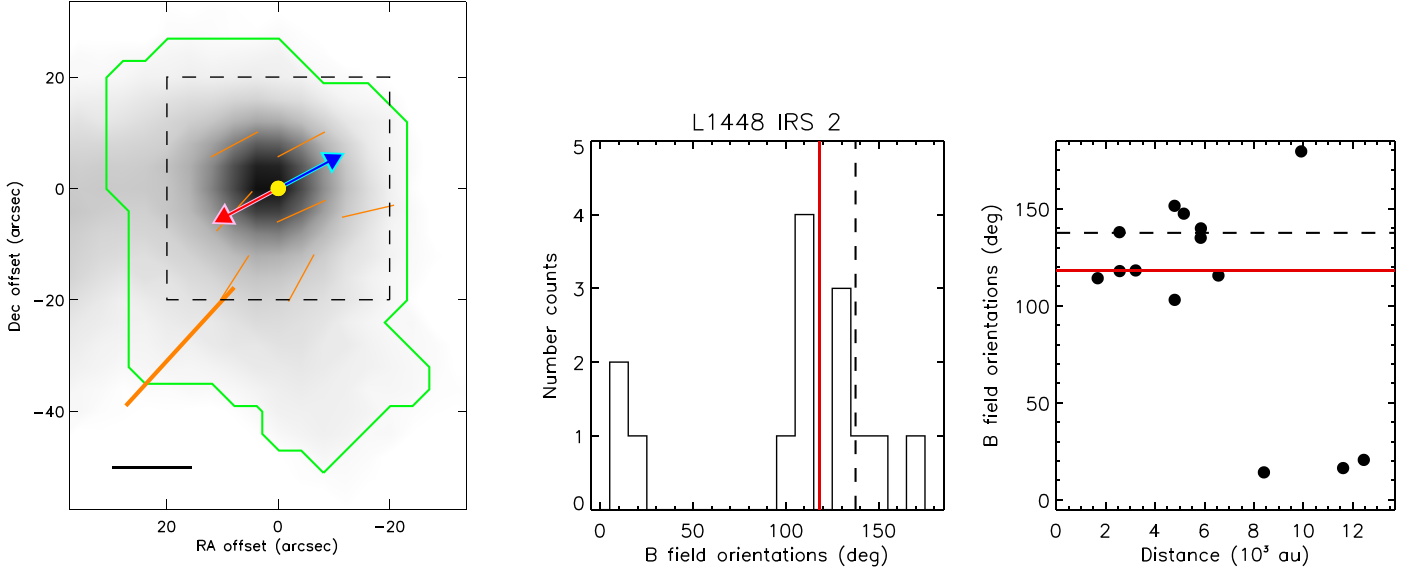
Figure 12. Same as Figures 3 and 4, but left panels only present the magnetic orientations (small orange segments) detected in the 40″ × 40″ regions (dashed open squares) around the sample protostars as well as the mean orientations of the magnetic field (long thick orange segments) in the individual dense cores/clumps. The complete magnetic field structures in these sources will be presented separately and discussed in detail in the forthcoming papers by the BISTRO team. Middle and right panels still present the number distributions of all the magnetic field orientations detected in the dense cores and clumps.

(The complete figure set (16 images) is available.)

Appendix D
Dependences of Misalignment on Source Properties

Figure 13 compares the measured misalignment angles with the sizes, total fluxes, mean intensities, and mean polarization percentages of the dense cores and the distances to the sources. The total flux and mean intensity are expected to be proportional to the total mass and mean column density of a dense core, respectively. These comparisons show that the measured misalignments do not depend on the mass and
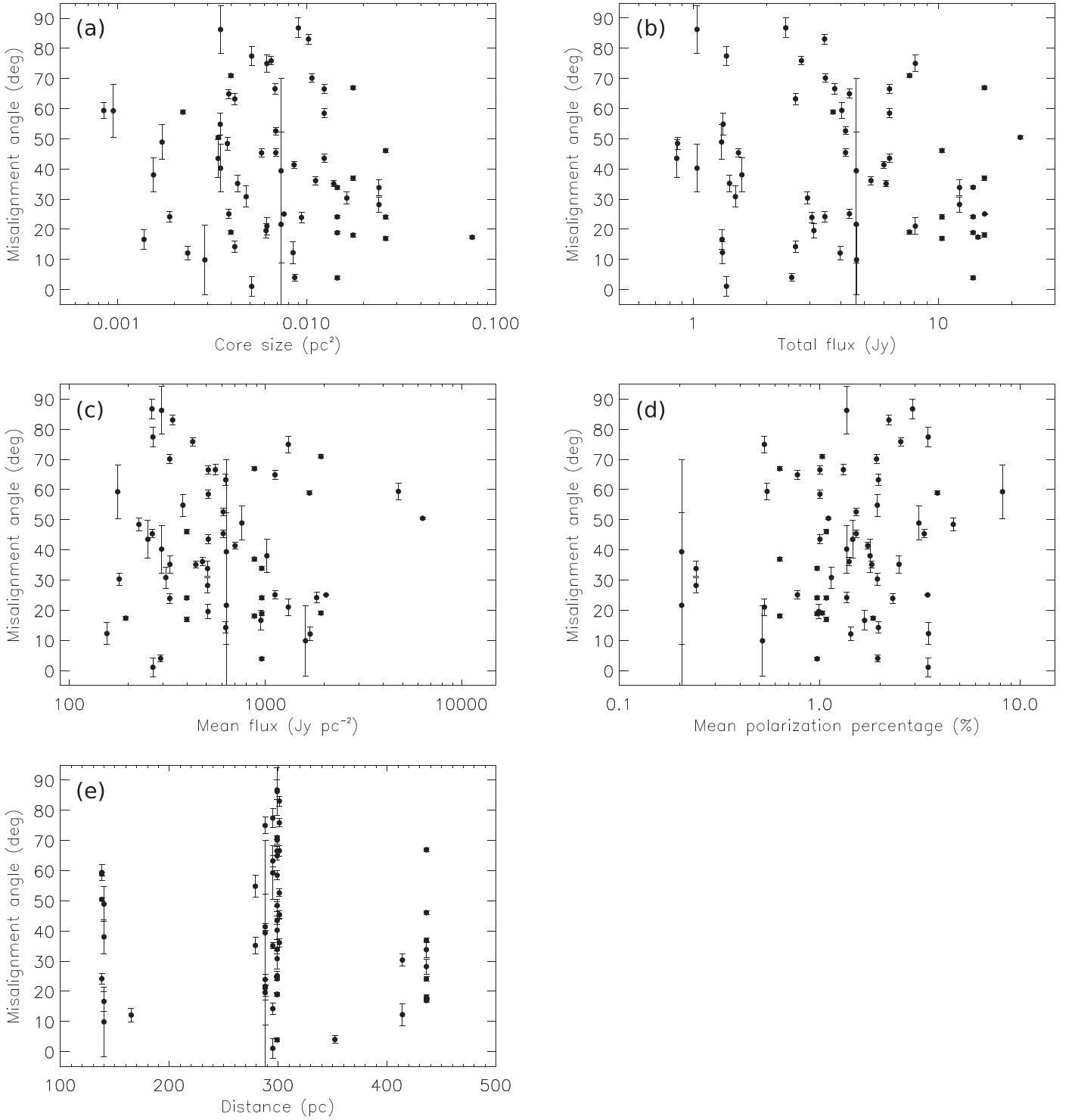
Figure 13. Misalignment angles as a function of (a) the size, (b) the total flux, (c) the mean intensity, (d) the mean polarization percentage, and (e) the distance of the dense cores. Error bars present the uncertainties in the mean magnetic field orientations from the error propagation of the uncertainties of the individual polarization detections. For several sources, the error bars are smaller than the symbol size. There is additional uncertainty in the misalignment angle due to the uncertainty in the outflow orientation, which is typically 10°.

density of the dense cores. We note that the magnetic field structures in the nearby sources can be better resolved than in the distant sources. The comparison also shows that the measured misalignments do not depend on the distances to the sources, even though the spatial resolutions are not uniform in the sample. Therefore, there is no bias due to the properties of the dense cores or the spatial resolutions in our results.

Appendix E
Comparison between JCMT and Interferometric Results

In 17 of our sample sources, the mean magnetic field orientations on a 1000 au scale were also measured with the CARMA, SMA, and/or ALMA observations (Hull et al. 2014; Galametz et al. 2018; Sadavoy et al. 2019). We compared the large- and small-scale misalignments measured with our JCMT
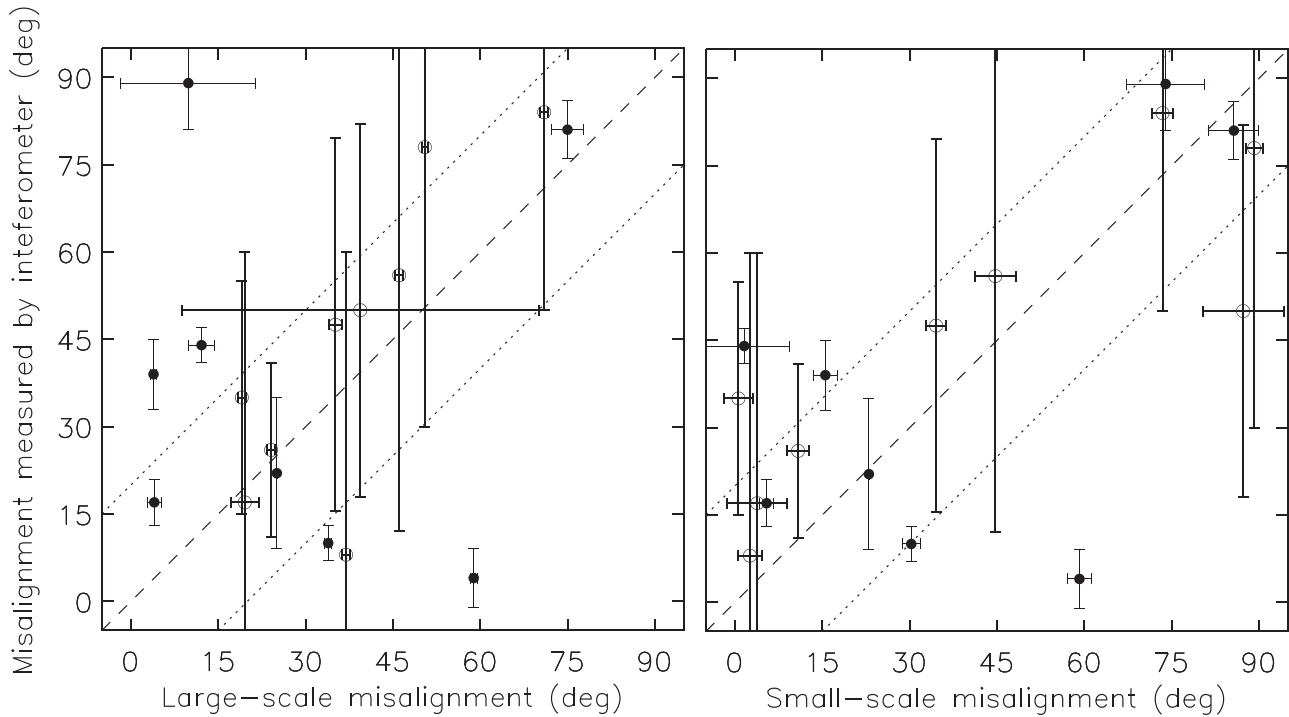
Figure 14. Comparison of the large- and small-scale misalignments measured with the JCMT observations with the misalignments on a 1000 au scale measured with the interferometric observations. The horizontal axes in the left and right panels show the large- and small-scale misalignments measured with JCMT, respectively. The vertical axes show the misalignment angles measured with the interferometer, and the results are obtained from Hull et al. (2014); Galametz et al. (2018), and Sadavoy et al. (2019). Open circles present the interferometric results from Hull et al. (2014), where the definition of the error bars is different, and their vertical error bars present the circular standard deviations of the observed magnetic field orientations. Dotted lines denote a difference in angle of ±20°.

POL-2 data and the misalignments measured with the interferometric data (Figure 14). The comparison with the large-scale misalignments measured with JCMT and the interferometric results show the same trend that in most of the sources the difference between the large- and small-scale magnetic field orientations is 10°–20°. In addition, our measured small-scale misalignments are correlated with the interferometric measurements. Thus, the magnetic field orientations close to the stellar positions observed with JCMT can represent the overall orientations of the magnetic field structures on a 1000 au scale in the protostellar sources.

ORCID iDs

Hsi-Wei Yen ● https://orcid.org/0000-0003-1412-893X
Patrick M. Koch ● https://orcid.org/0000-0003-2777-5861
Charles L. H. Hull ● https://orcid.org/0000-0002-8975-7573
Derek Ward-Thompson ● https://orcid.org/0000-0003-1140-2761
Tetsuo Hasegawa ● https://orcid.org/0000-0003-1853-0184
Woojin Kwon ● https://orcid.org/0000-0003-4022-4132
Shih-Ping Lai ● https://orcid.org/0000-0001-5522-486X
Keping Qiu ● https://orcid.org/0000-0002-5093-5088
Tao-Chung Ching ● https://orcid.org/0000-0001-8516-2532
Eun Jung Chung ● https://orcid.org/0000-0003-0014-1527
Simon Coudé ● https://orcid.org/0000-0002-0859-0805
Yasuo Doi ● https://orcid.org/0000-0001-8746-6548
Chakali Eswaraiah ● https://orcid.org/0000-0003-4761-6139
Gary Fuller ● https://orcid.org/0000-0001-8509-1818
Ray S. Furuya ● https://orcid.org/0000-0003-0646-8782
Jennifer Hatchell ● https://orcid.org/0000-0002-4870-2760
Martin Houde ● https://orcid.org/0000-0003-4420-8674
Shu-ichiro Inutsuka ● https://orcid.org/0000-0003-4366-6518
Doug Johnstone ● https://orcid.org/0000-0002-6773-459X
Ji-hyun Kang ● https://orcid.org/0000-0001-7379-6263
Miju Kang ● https://orcid.org/0000-0002-5016-050X
Kee-Tae Kim ● https://orcid.org/0000-0003-2412-7092
Florian Kirchschlager ● https://orcid.org/0000-0002-3036-0184
Jungmi Kwon ● https://orcid.org/0000-0003-2815-7774
Chin-Fei Lee ● https://orcid.org/0000-0002-3024-5864
Hong-Li Liu ● https://orcid.org/0000-0003-3343-9645
Tie Liu ● https://orcid.org/0000-0002-5286-2564
A-Ran Lyo ● https://orcid.org/0000-0002-9907-8427
Takashi Onaka ● https://orcid.org/0000-0002-8234-6747
Kate Pattle ● https://orcid.org/0000-0002-8557-3582
Sarah Sadavoy ● https://orcid.org/0000-0001-7474-6874
Hiroko Shinnaga ● https://orcid.org/0000-0001-9407-6775
Archana Soam ● https://orcid.org/0000-0002-6386-2906
Motohide Tamura ● https://orcid.org/0000-0002-6510-0681
Ya-Wen Tang ● https://orcid.org/0000-0002-0675-276X
Xindi Tang ● https://orcid.org/0000-0002-4154-4309
Chuan-Peng Zhang ● https://orcid.org/0000-0002-4428-3183

References

Allen, A., Li, Z.-Y., & Shu, F. H. 2003, ApJ, 599, 363
Ansdell, M., Williams, J. P., Trapman, L., et al. 2018, ApJ, 859, 21
Arce, C., Louvet, F., Cortes, P., et al. 2020, A&A, 640, A111
Aso, Y., Hirano, N., Aikawa, Y., et al. 2019, ApJ, 887, 209
Bachiller, R., Pérez Gutiérrez, M., Kumar, M. S. N., et al. 2001, A&A, 372, 899
Basu, S., & Mouschovias, T. C. 1994, ApJ, 432, 720
Blandford, R. D., & Payne, D. G. 1982, MNRAS, 199, 883
Burkert, A., & Bodenheimer, P. 2000, ApJ, 543, 822
Chapman, N. L., Davidson, J. A., Goldsmith, P. F., et al. 2013, ApJ, 770, 151
Chen, C.-Y., Behrens, E. A., Washington, J. E., et al. 2020, MNRAS, 494, 1971

Chen, C.-Y., & Ostriker, E. C. 2014, ApJ, 785, 69
Chen, C.-Y., & Ostriker, E. C. 2015, ApJ, 810, 126
Chen, C.-Y., & Ostriker, E. C. 2018, ApJ, 865, 34
Chen, H., Myers, P. C., Ladd, E. F., et al. 1995, ApJ, 445, 377
Ciardi, A., & Hennebelle, P. 2010, MNRAS, 409, L39
Cieza, L. A., Ruíz-Rodríguez, D., Hales, A., et al. 2019, MNRAS, 482, 698
Coudé, S., Bastien, P., Houde, M., et al. 2019, ApJ, 877, 88
Cox, E. G., Harris, R. J., Looney, L. W., et al. 2018, ApJ, 855, 92
Crapsi, A., van Dishoeck, E. F., Hogerheijde, M. R., et al. 2008, A&A, 486, 245
Crutcher, R. M. 2012, ARA&A, 50, 29
Crutcher, R. M., Wandelt, B., Heiles, C., et al. 2010, ApJ, 725, 466
Currie, M. J., Berry, D. S., Jenness, T., et al. 2014, in ASP Conf. Ser. 485, Astronomical Data Analysis Software and Systems XXIII, ed. N. Manset & P. Forshay (San Francisco, CA: ASP), 391
Davidson, J. A., Novak, G., Matthews, T. G., et al. 2011, ApJ, 732, 97
Dib, S., Hennebelle, P., Pineda, J. E., et al. 2010, ApJ, 723, 425
Doi, Y., Hasegawa, T., Furuya, R. S., et al. 2020, ApJ, 899, 28
Dunham, M. M., Crapsi, A., Evans, N. J., et al. 2008, ApJS, 179, 249
Enoch, M. L., Evans, N. J., Sargent, A. I., et al. 2008, ApJ, 684, 1240
Evans, N. J., Dunham, M. M., Jørgensen, J. K., et al. 2009, ApJS, 181, 321
Friberg, P., Bastien, P., Berry, D., et al. 2016, Proc. SPIE, 9914, 991403
Friesen, R. K., Pon, A., Bourke, T. L., et al. 2018, ApJ, 869, 158
Galametz, M., Maury, A., Girart, J. M., et al. 2018, A&A, 616, A139
Galli, D., & Shu, F. H. 1993, ApJ, 417, 220
Gammie, C. F., Lin, Y.-T., Stone, J. M., et al. 2003, ApJ, 592, 203
Gaudel, M., Maury, A. J., Belloche, A., et al. 2020, A&A, 637, A92
Girart, J. M., Rao, R., & Marrone, D. P. 2006, Sci, 313, 812
Gray, W. J., McKee, C. F., & Klein, R. I. 2018, MNRAS, 473, 2124
Haisch, K. E., Lada, E. A., & Lada, C. J. 2001, ApJL, 553, L153
Hirano, S., Tsukamoto, Y., Basu, S., et al. 2020, ApJ, 898, 118
Holland, W. S., Bintley, D., Chapin, E. L., et al. 2013, MNRAS, 430, 2513
Hsieh, T.-H., Lai, S.-P., & Belloche, A. 2017, AJ, 153, 173
Hull, C. L. H., Girart, J. M., Tychoniec, Ł., et al. 2017, ApJ, 847, 92
Hull, C. L. H., Gouellec, V. J. M. L., Girart, J. M., et al. 2020, ApJ, 892, 152
Hull, C. L. H., Plambeck, R. L., Bolatto, A. D., et al. 2013, ApJ, 768, 159
Hull, C. L. H., Plambeck, R. L., Kwon, W., et al. 2014, ApJS, 213, 13
Hull, C. L. H., & Zhang, Q. 2019, FrASS, 6, 3
Joos, M., Hennebelle, P., & Ciardi, A. 2012, A&A, 543, A128
Joos, M., Hennebelle, P., Ciardi, A., et al. 2013, A&A, 554, A17
Kamazaki, T., Nakamura, F., Kawabe, R., et al. 2019, ApJ, 871, 86
Ko, C.-L., Liu, H. B., Lai, S.-P., et al. 2020, ApJ, 889, 172
Koch, P. M., Tang, Y.-W., Ho, P. T. P., et al. 2014, ApJ, 797, 99
Kristensen, L. E., van Dishoeck, E. F., Bergin, E. A., et al. 2012, A&A, 542, A8
Krumholz, M. R., Crutcher, R. M., & Hull, C. L. H. 2013, ApJL, 767, L11
Kuznetsova, A., Hartmann, L., & Heitsch, F. 2020, ApJ, 893, 73
Kwon, J., Doi, Y., Tamura, M., et al. 2018, ApJ, 859, 4
Kwon, W., Stephens, I. W., Tobin, J. J., et al. 2019, ApJ, 879, 25
Lam, K. H., Li, Z.-Y., Chen, C.-Y., et al. 2019, MNRAS, 489, 5326
Le Gouellec, V. J. M., Hull, C. L. H., Maury, A. J., et al. 2019, ApJ, 885, 106
Lee, C.-F., Ho, P. T. P., Li, Z.-Y., et al. 2017b, Nature Astronomy, 1, 0152
Lee, C.-F., Hwang, H.-C., & Li, Z.-Y. 2016, ApJ, 826, 213
Lee, C.-F., Kwon, W., Jhan, K.-S., et al. 2019, ApJ, 879, 101
Lee, J. W. Y., Hull, C. L. H., & Offner, S. S. R. 2017a, ApJ, 834, 201
Li, P. S., Norman, M. L., Mac Low, M.-M., et al. 2004, ApJ, 605, 800
Li, Z.-Y., Banerjee, R., Pudritz, R. E., et al. 2014, in Protostars and Planets VI, ed. H Beuther et al. (Tucson, AZ: Univ. Arizona Press), 173
Li, Z.-Y., Krasnopolsky, R., & Shang, H. 2013, ApJ, 774, 82
Liu, J., Qiu, K., Berry, D., et al. 2019, ApJ, 877, 43
Masson, J., Chabrier, G., Hennebelle, P., Vaytet, N., & Commerçon, B. 2016, A&A, 587, A32
Matsumoto, T., Machida, M. N., & Inutsuka, S. 2017, ApJ, 839, 69
Matthews, B. C., McPhee, C. A., Fissel, L. M., et al. 2009, ApJS, 182, 143
Maury, A. J., André, P., Testi, L., et al. 2019, A&A, 621, A76
Maury, A. J., Girart, J. M., Zhang, Q., et al. 2018, MNRAS, 477, 2760
McKee, C. F., & Ostriker, E. C. 2007, ARA&A, 45, 565

Mellon, R. R., & Li, Z.-Y. 2008, ApJ, 681, 1356
Menten, K. M., Reid, M. J., Forbrich, J., et al. 2007, A&A, 474, 515
Motte, F., & André, P. 2001, A&A, 365, 440
Mouschovias, T. C., & Paleologou, E. V. 1979, ApJ, 230, 204
Murillo, N. M., Lai, S.-P., Bruderer, S., et al. 2013, A&A, 560, A103
Nakano, T., & Nakamura, T. 1978, PASJ, 30, 671
Ngoc, B., Diep, P. M., Parsons, H., et al. 2020, ApJ, in press (arXiv:2012.04297)
Ortiz-León, G. N., Loinard, L., Dzib, S. A., et al. 2018a, ApJL, 869, L33
Ortiz-León, G. N., Loinard, L., Dzib, S. A., et al. 2018b, ApJ, 865, 73
Palmeirim, P., André, P., Kirk, J., et al. 2013, A&A, 550, A38
Pattle, K., & Fissel, L. 2019, FrASS, 6, 15
Pattle, K., Lai, S.-P., Hasegawa, T., et al. 2019, ApJ, 880, 27
Pattle, K., Ward-Thompson, D., Berry, D., et al. 2017, ApJ, 846, 122
Pattle, K., Ward-Thompson, D., Hasegawa, T., et al. 2018, ApJL, 860, L6
Piétu, V., Dutrey, A., & Guilloteau, S. 2007, A&A, 467, 163
Planck Collaboration, Adam, R., Ade, P. A. R., et al. 2016a, A&A, 586, A135
Planck Collaboration, Ade, P. A. R., Aghanim, N., et al. 2015, A&A, 576, A104
Planck Collaboration, Ade, P. A. R., Aghanim, N., et al. 2016b, A&A, 586, A138
Poidevin, F., Falceta-Gonçalves, D., Kowal, G., et al. 2013, ApJ, 777, 112
Pudritz, R. E., & Norman, C. A. 1983, ApJ, 274, 677
Rao, R., Girart, J. M., Lai, S.-P., et al. 2014, ApJL, 780, L6
Sadavoy, S. I., Myers, P. C., Stephens, I. W., et al. 2018, ApJ, 859, 165
Sadavoy, S. I., Stephens, I. W., Myers, P. C., et al. 2019, ApJS, 245, 2
Santangelo, G., Murillo, N. M., Nisini, B., et al. 2015, A&A, 581, A91
Simon, M., Guilloteau, S., Di Folco, E., et al. 2017, ApJ, 844, 158
Soam, A., Lee, C. W., Andersson, B.-G., et al. 2019, ApJ, 883, 9
Soam, A., Pattle, K., Ward-Thompson, D., et al. 2018, ApJ, 861, 65
Soler, J. D., Hennebelle, P., Martin, P. G., et al. 2013, ApJ, 774, 128
Stephens, I. W., Dunham, M. M., Myers, P. C., et al. 2017, ApJ, 846, 16
Stephens, I. W., Looney, L. W., Kwon, W., et al. 2013, ApJL, 769, L15
Tafalla, M., Bachiller, R., Lefloch, B., et al. 2015, A&A, 573, L2
Tafalla, M., Liseau, R., Nisini, B., et al. 2013, A&A, 551, A116
Takahashi, S., Ohashi, N., & Bourke, T. L. 2013, ApJ, 774, 20
Takakuwa, S., Tsukamoto, Y., Saigo, K., et al. 2018, ApJ, 865, 51
Tobin, J. J., Looney, L. W., Li, Z.-Y., et al. 2016, ApJ, 818, 73
Tobin, J. J., Sheehan, P., Megeath, S. T., et al. 2020, ApJ, 890, 130
Torres, R. M., Loinard, L., Mioduszewski, A. J., et al. 2009, ApJ, 698, 242
Tsukamoto, Y., Okuzumi, S., Iwasaki, K., et al. 2017, PASJ, 69, 95
Tychoniec, Ł., Hull, C. L. H., Kristensen, L. E., et al. 2019, A&A, 632, A101
van Kempen, T. A., van Dishoeck, E. F., Salter, D. M., et al. 2009, A&A, 498, 167
Verliat, A., Hennebelle, P., Maury, A. J., et al. 2020, A&A, 635, A130
Wang, J.-W., Lai, S.-P., Eswaraiah, C., et al. 2019a, ApJ, 876, 42
Wang, L.-Y., Shang, H., & Chiang, T.-Y. 2019b, ApJ, 874, 31
Ward-Thompson, D., Pattle, K., Bastien, P., et al. 2017, ApJ, 842, 66
Watson, D. M. 2020, RNAAS, 4, 88
Williams, J. P., Cieza, L., Hales, A., et al. 2019, ApJL, 875, L9
Williams, J. P., & Cieza, L. A. 2011, ARA&A, 49, 67
Williams, J. P., de Geus, E. J., & Blitz, L. 1994, ApJ, 428, 693
Wolf, S., Launhardt, R., & Henning, T. 2003, ApJ, 592, 233
Wurster, J., & Bate, M. R. 2019, MNRAS, 486, 2587
Wurster, J., Bate, M. R., & Price, D. J. 2019, MNRAS, 489, 1719
Yen, H.-W., Koch, P. M., Manara, C. F., et al. 2018, A&A, 616, A100
Yen, H.-W., Koch, P. M., Takakuwa, S., et al. 2015, ApJ, 799, 193
Yen, H.-W., Zhao, B., Hsieh, I.-T., et al. 2019, ApJ, 871, 243
Yen, H.-W., Zhao, B., Koch, P., et al. 2020, ApJ, 893, 54
Young, C. H., & Evans, N. J. 2005, ApJ, 627, 293
Young, C. H., Shirley, Y. L., Evans, N. J., et al. 2003, ApJS, 145, 111
Zhang, Q., Qiu, K., Girart, J. M., et al. 2014, ApJ, 792, 116
Zhang, S., Hartmann, L., Zamora-Avilés, M., et al. 2018, MNRAS, 480, 5495
Zhao, B., Caselli, P., Li, Z.-Y., et al. 2016, MNRAS, 460, 2050
Zhao, B., Caselli, P., Li, Z.-Y., & Krasnopolsky, R. 2018, MNRAS, 473, 4868
Zucker, C., Speagle, J. S., Schlafly, E. F., et al. 2019, ApJ, 879, 125